

Hypersensitivity of Southern Ocean air-sea carbon fluxes to background turbulent diapycnal mixing

Elizabeth Catherine Ellison¹, Ali Mashayek², and Matthew R. Mazloff³

¹Imperial College london

²Imperial College London

³UCSD

March 1, 2023

Abstract

The Southern Ocean (SO) is the worlds largest high nutrient low chlorophyll region and has a plentiful supply of underutilised macronutrients due to light and iron limitation. These macronutrients supply the rest of the neighboring ocean basins, and are hugely important for global productivity and ocean carbon sequestration. Vertical mixing rates in the SO are known to vary by an order of magnitude temporally and spatially, however there is great uncertainty in the parameterization of this mixing, including in the specification of a background mixing value in coarse resolution Earth System Models. Using a biogeochemical-ocean model we show that SO biomass is highly sensitive to altering the background diapycnal mixing over short timescales. Increasing mixing enhances biomass by altering key biogeochemical and physical parameters. An increased surface supply of iron is responsible for biomass increases in most areas, demonstrating the importance of year round diapycnal fluxes of iron to SO surface waters. These changes to SO biomass could potentially alter atmospheric CO₂ concentration over longer timescales, demonstrating the importance of accurate representation of diapycnal mixing in climate models.

1
2

3

4
5
6

7
8
9
10
11
12
13

Hypersensitivity of Southern Ocean air-sea carbon fluxes to background turbulent diapycnal mixing

Elizabeth Ellison¹, Ali Mashayek², Matthew Mazloff³

¹Imperial College London, Department of Civil and Environmental Engineering, London, UK
²University of Cambridge, Department of Earth Sciences, Cambridge, UK
³Scripps Institute of Oceanography, University of California San Diego, La Jolla, USA

Key Points:

- Total air-sea carbon fluxes in the Southern Ocean are altered by up to 66% annually by modest background mixing variations.
- Resolving or skillfully parameterising the spatiotemporal variability of small-scale turbulent mixing in the Southern Ocean is essential to model air-sea carbon fluxes.
- The spatiotemporal coverage of available $p\text{CO}_2$ observations is insufficient for constraining the role of diapycnal mixing rates below the mixed layer on air-sea fluxes

Abstract

The Southern Ocean (SO) connects major ocean basins and hosts large air-sea carbon fluxes due to the resurfacing of deep nutrient and carbon-rich waters. While surface-intensified wind-induced turbulent mixing in the SO surface mixed layer is significant for air-sea fluxes, the orders-of-magnitude weaker background mixing below the mixed layer has not been considered consequential. Topographically induced upward propagating lee waves in the SO, wind-induced downward propagating waves generated at the base of the mixed layer, shoaling of southward propagating internal tides generated in the basins north of the SO, and turbulence under sea ice are among the processes known to induce upper ocean background turbulence but typically are not represented in models. Here, we show that altering the background mixing in the SO over a modest range can lead to a $\sim 40\%$ - 60% annual change in SO air-sea CO_2 fluxes, with bigger changes on a seasonal timescale. This is primarily through altering the temperature and the dissolved inorganic carbon and alkalinity distribution in the surface water. Given the high spatiotemporal variability of processes that induce small-scale background mixing, this work demonstrates the importance of their representation in climate models for accurate simulation of global biogeochemical cycles.

Introduction

The Southern Ocean (SO), defined here as any region south of 30°S , is a key region for the global carbon cycle due to the upwelling of deep, old, carbon and nutrient-enriched waters, connecting the vast reservoir of nutrients and carbon from below the mixed layer with the surface (Talley et al., 2016). The deep ocean interacts with the atmosphere through less than 4% of the ocean's surface area (Watson & Naveira Garabato, 2006; Klocker, 2018), with 65% of interior waters making first contact with the atmosphere in the SO (DeVries & Primeau, 2011). As the deep ocean contains up to 60 times more carbon than the atmosphere (Arias et al., 2021), small perturbations to air-sea carbon fluxes can be important for atmospheric carbon content (Adkins, 2013). Therefore, the SO, and especially the upwelling branch of circumpolar deep water (Marshall & Speer, 2012), is key in controlling global biogeochemical cycles, the exchange of CO_2 between the atmosphere and the deep ocean, atmospheric CO_2 levels, and the response of the ocean and atmosphere to climate change (Sarmiento et al., 2004; Gruber et al., 2019).

Several expeditions have revealed strong cross-density (diapycnal) mixing due to small-scale ocean turbulence in the SO (Garabato et al., 2004; Ledwell et al., 2011; Watson et al., 2013; Garabato et al., 2019), though measurements remain sparse and difficult to scale up (Tamsitt et al., 2018; Mashayek et al., 2017; Cael & Mashayek, 2021; Mashayek et al., 2022). Given the small scales of diapycnal mixing, it is not resolved in operational models, and so it is parameterised (Gaspar, Grégoris, & Lefevre, 1990; W. G. Large et al., 1994) in two forms:

1. Surface mixed layer mixing from storms and other surface winds, as well as convective instabilities.
2. Background turbulence induced by bottom generated internal waves due to interaction of jets, eddies, and tides with rough topography or due to shoaling and breaking of remotely generated internal tides (see de Lavergne et al. (2020); Baker and Mashayek (2021, 2022) for reviews of such dynamics).

The ‘background’ mixing in the ocean interior is typically several orders of magnitude smaller than that in the surface mixed layers. Since the seminal work of Munk (1966), bulk measurements of ocean mixing have found a diapycnal turbulent diffusivity of $K_v \sim \mathcal{O}(10^{-4}) \text{ m}^2 \text{ s}^{-1}$ required to resurface the abyssal waters and facilitate the closure of the meridional overturning circulation (MOC) (Ganachaud & Wunsch, 2000; Talley et al., 2003; Lumpkin & Speer, 2007; Talley, 2013), while estimates from profiling instruments often find $K_v \sim \mathcal{O}(10^{-5}) \text{ m}^2 \text{ s}^{-1}$ in the interior of the ocean and much larger values only very close to

the seafloor (Waterhouse et al., 2014; Ferrari, 2014). In the Diapycnal and Isopycnal Mixing Experiment in the Southern Ocean (DIMES), estimates of mixing based on microstructure profiles reported $K_v \sim \mathcal{O}(10^{-5})m^2 s^{-1}$ at the mean depth of an anthropogenic tracer released upstream of the Drake Passage. Meanwhile, the tracer itself appeared to experience $K_v \sim \mathcal{O}(10^{-4})m^2 s^{-1}$ (Watson et al., 2013; Mashayek et al., 2017). The background values used in models typically lie within this range.

Though diapycnal mixing is highly temporally and spatially variable due to its generating mechanisms (e.g. strong surface westerly winds and interaction of the currents and eddies with rough topography), it is frequently parameterised as temporally invariable and, at times, even spatially constant. Current best estimates of SO diapycnal mixing are based on ‘static’ maps, produced with numerous limiting assumptions, approximating the contributions from topographically generated lee waves (Nikurashin & Ferrari, 2011; Shakespeare, 2020), wind-induced near-inertial waves (Alford, 2020), and internal tides (de Lavergne et al., 2020). These maps have formed the basis of our representation of such processes in earth system models (A. Melet et al., 2014; A. V. Melet et al., 2022).

Diapycnal mixing in the global ocean interior is known to be an important factor in variations in atmospheric carbon levels on centennial to millennial timescales via alterations in ocean circulation (Sigman et al., 2010; Marinov & Gnanadesikan, 2011). Enhanced diapycnal mixing increases deep ocean ventilation via the SO and reduces ocean carbon storage through biological and solubility carbon pumps (Marinov et al., 2008; Marinov & Gnanadesikan, 2011). Climate models are sensitive to the intensity and distribution of global diapycnal mixing, accounting for about 25% of the uncertainty in the estimated range of atmospheric CO_2 concentrations by 2100 (Schmittner et al., 2009). In this work, we are concerned with the response of the air-sea carbon fluxes to mixing below the surface mixed layer on time scales much shorter than those explored in the abovementioned works. We also solely focus on mixing in the SO which has been assumed to be of secondary importance for the global ocean circulation (Nikurashin & Ferrari, 2013) but significant for setting global tracer distributions (Ellison et al., 2021).

Given the strong wind-driven isopycnal upwelling in the Southern Ocean, and the intense diapycnal mixing within the mixed layer induced by strong winds, one may imagine that the modest background mixing below the mixed layer would be inconsequential for setting the air-sea fluxes of CO_2 on short timescales. In this work, we show the contrary. The air-sea flux of CO_2 primarily depends on the difference in the partial pressures of CO_2 (pCO_2) between the atmosphere and the ocean. Physical and biological processes, including advective and diffusive transport of tracers, organic matter formations and sinking, and the dilution of tracers due to precipitation, runoff and sea ice melt, all alter the pCO_2 of surface waters (Mahadevan et al., 2011), resulting in high variability in time and space of the CO_2 fluxes in the SO (Rosso et al., 2017). The influence of altering background diapycnal mixing on the surface ocean pCO_2 is complex to predict due to spatiotemporal variability in biological and physical responses to variations in mixing (Dutreuil et al., 2009), and the coupled multivariate dependency of ocean pCO_2 to temperature, salinity, alkalinity and dissolved inorganic carbon. In this work, we will show that modest perturbation of the background mixing strongly alters the SO-integrated air-sea CO_2 fluxes on seasonal, annual, and interannual timescales.

Experiment Setup

We use the Biogeochemical Southern Ocean state estimate (B-SOSE; Verdy and Mazloff (2017)). The interaction between diapycnal mixing below the mixed layer, the mixed layer dynamics, and the mesoscale processes that advect tracers prove essential for the problem under consideration here. Thus, employing an eddy-resolving model such as B-SOSE is essential and distinguishes this work from studies mentioned earlier that use low-resolution

models in global settings to study the role of mixing on carbon fluxes. In return, the timescales of relevance in our study are much shorter than theirs.

The model’s optimization procedure solves for adjustments to the prescribed atmospheric state and initial conditions to bring the solution into better consistency with observations. The resulting product is a closed-budget model simulation representing the present SO state. Because it represents the constantly evolving SO state it is not in a steady state, in contrast to what one may expect from analysis of an earth system model undergoing a long spin-up process. The B-SOSE simulation provides an estimate of SO biogeochemistry, including air-sea fluxes of heat and carbon and the cycling of nutrients from a biogeochemical and carbon model.

The model domain extends from the equator to 78°S with 52 vertical layers of varying thickness. The zonal grid spacing is always $1/6^\circ$, but the meridional grid spacing changes with the cosine of the latitude. Ocean physics is represented using the MITgcm. The ocean is forced through an atmospheric boundary layer scheme where bulk formulae determine heat fluxes, freshwater (salt), and momentum (W. Large & Yeager, 2009). The hourly atmospheric conditions of ERA5 (Dee et al., 2011) are applied, with adjustments added that were determined by optimization (Verdy & Mazloff, 2017) using the adjoint method. Sea ice is modelled using 0-layer thermodynamics (Fenty & Heimbach, 2013) and an implicit Line Successive Over Relaxation (LSOR) dynamical solver (Losch et al., 2010). A horizontal biharmonic diffusivity is used with a value of $10^{-8} \text{ m}^4\text{s}^{-1}$. Implicit vertical diffusivity for convection is set to $10 \text{ m}^2\text{s}^{-1}$, and no mesoscale eddy parameterisation was implemented. For further details, see Verdy and Mazloff (2017) and Swierczek et al. (2021).

The parameterisation of diapycnal mixing is composed of two parts. The GGL90 mixed layer parameterisation of Gaspar, Grégoris, and Lefevre (1990) is used to represent parameterised turbulence and is highly surface-enhanced (Fig.1 D), inducing strong turbulence under the seasonal atmospheric storm tracks, mixing the DIC gradients in the upper few hundreds of meters. In other places, such as under the ice or when there is no strong wind-induced turbulence, the models rely on a prescribed background value for turbulent diffusivity. The background value is behind the sensitivity of fluxes discussed in this work. As discussed in subsequent paragraphs, the background vertical diffusivity is altered in each experimental run. The background mixing value is added to the GGL90 mixing to achieve a total vertical diapycnal mixing value.

The Biogeochemistry with LIght, Nutrients and Gases (NBLING) model, described fully in Verdy and Mazloff (2017), forms the biochemical framework within B-SOSE. The original BLING model described in Galbraith et al. (2010) was modified (for B-SOSE) with the addition of nitrogen cycling and improvements in the representation of phytoplankton population dynamics and particle export (Galbraith et al., 2015; Bianchi et al., 2013). Biological activity influences the concentrations of carbon and oxygen. At the core of the BLING model is primary production with limitations by light, nitrate, phosphate, iron, and temperature, and subsequent remineralization of organic matter back to inorganic nutrients. Nine prognostic tracers are simulated in NBLING: dissolved inorganic carbon (DIC), alkalinity (ALK), oxygen (O_2), nitrate (NO_3), phosphate (PO_4), iron (Fe), dissolved organic nitrogen (DON), dissolved organic phosphate (DOP) and phytoplankton biomass. The biomass partitioning into species is determined using stored ratios updated every timestep based on growth and decay rates. We include three types of phytoplankton: large, small, and diazotrophs. Small cells represent calcifying organisms; they use calcium carbonate to form shells. Diazotrophs can fix nitrogen, so nitrate availability does not limit them. Phytoplankton loss is expressed as a power law with a size-dependent exponent based on (Dunne et al., 2005).

The B-SOSE carbon system is adapted from the MITgcm simple biogeochemical model of Dutkiewicz et al. (2006). DIC and ALK are prognostic variables, and pH and $p\text{CO}_2$ are diagnosed based on Follows et al. (2006), making oceanic $p\text{CO}_2$ a function of DIC,

ALK, temperature (T), salinity (S) and silica, where silica is prescribed from the 2013 World Ocean Atlas climatology (Garcia et al., 2013). CO₂ and oxygen air-sea fluxes are calculated following Wanninkhof (1992). Atmospheric $p\text{CO}_2$ is prescribed using values from the CarbonTracker product (Peters et al., 2007).

The state estimate is produced by solving for the model initial and boundary conditions, the so-called model ‘controls’, which minimize a weighted least squares sum of model-observation misfits. This is achieved using an adjoint model that provides the gradients of the misfit function with respect to the model controls, allowing those controls to be efficiently and systematically determined. The model is run for seven years (2012 - 2018) using the adjoint method-based assimilation product. This includes physical and biogeochemical constraints obtained from Argo floats, including biogeochemical parameters from the SOCCOM float array, satellite altimetry, satellite SST, and ship transect data. The full set of model parameters used in this 1/6° setup is given in Swierczek et al. (2021); see Verdy and Mazloff (2017) for initial conditions.

The B-SOSE’s original conditions and atmospheric adjustments were obtained using $10^{-4} \text{ m}^2 \text{ s}^{-1}$ as the value for background diapycnal diffusivity (added to the GGL90 mixing). We refer to that base simulation as Ex1e-4 hereafter. Using the same initial conditions and atmospheric state adjustments, two additional model simulations were carried out for 2013-2018. The first perturbation experiment, Ex1e-5, uses a constant background diffusivity value of $10^{-5} \text{ m}^2 \text{ s}^{-1}$. The range $10^{-5} \text{ m}^2 \text{ s}^{-1}$ to $10^{-4} \text{ m}^2 \text{ s}^{-1}$ is conservative, sandwiched between the two canonical paradigms of mixing often considered in Physical Oceanography. The third experiment, ExVar, uses a spatially variable (but temporally constant) vertical diapycnal mixing map (Fig 1A-C). The map is constructed as the sum of contributions from tides (de Lavergne et al., 2020) and topographically-generated lee waves (Nikurashin & Ferrari, 2013). ExVar features horizontal and vertical variations over a range much broader than $10^{-5} \text{ m}^2 \text{ s}^{-1}$ to $10^{-4} \text{ m}^2 \text{ s}^{-1}$. Although background mixing values dominate over the GGL90 parameterisation in mid-depths, GGL90 is orders of magnitude larger than the background mixing value in the upper ocean (Fig.1D). The three cases together allow for evaluating the impact of the magnitude of mixing and its spatial variations on the carbon flux independently.

Results

Carbon fluxes

The SO is a net sink of atmospheric CO₂, with most of the uptake occurring between 50°S and 30°S, with a peak at 40°S, where around 7 Tg C/yr is taken up (Fig.2A). 40°S is the average latitude of the subtropical front, separating the subtropical waters from the subantarctic mode waters, thus hosting rich mesoscale and submesoscale frontal dynamics and enhanced air-sea exchange of tracers. To the south of the polar front (panel E), on the other hand, the upwelling of deep carbon-rich waters causes carbon outgassing (shown in red panel E). Additional uptake occurs further south around Antarctica due to downwelling (induced by a change in the wind direction from westerly to easterly) and deep water formation. Thus, SO fronts, which mark sharp gradients in temperature and carbon chemistry, separate regions of net uptake from regions of outgassing. Higher latitudes show very low mean annual carbon fluxes, partly due to seasonal ice cover.

Carbon uptake varies year-on-year during the six years of the state estimate run by almost 2 Tg C/yr at some latitudes, with especially high inter-annual variability at 60°S and 40°S (Fig.2A). The inter-annual range of carbon fluxes for Ex1e-5 are highly non-monotonic. The inter-annual variations are due to varying oceanic conditions each year, some of which are associated with the Southern Annular Mode (SAM).

Alterations to background diapycnal mixing alter SO carbon fluxes, with ExVar showing smaller differences from Ex1e-5 than Ex1e-4 (Fig.2B dashed vs solid lines). The sensitivity

to altered diapycnal mixing is variable throughout the six years (Fig.2 B). This inter-annual range in sensitivity of around 0.1 Tg C/yr is well within the range of the inter-annual variability of zonally integrated carbon fluxes in Ex1e-5 (Fig.2A,B). A higher difference between Ex1e-5 and Ex1e-4, and to a lesser extent between Ex1e-5 and ExVar occurs in the first three years (2013 to 2015) than in the last three years (2016 to 2018) (Fig.2B). As upper ocean mixing is never in an equilibrium state due to constantly changing winds, eddies and buoyancy fluxes, the response to the mixing perturbation over the first few months of this experiment do not seem unrealistically exaggerated .

Increasing the background mixing from Ex1e-5 to Ex1e-4 leads to a reduction in annual mean zonally integrated carbon uptake at all latitudes (Fig.2C,F). The most significant reduction is around 55°S (Fig.2C,F). Minor changes occur south of 65°S due to the ice cover. In ExVar, the most significant changes from Ex1e-5 occur further north, at around 45°S. South of 60°S, the difference between ExVar and Ex1e-5 is insignificant (Fig.2C,G). Large areas of ExVar have carbon fluxes unchanged from those in Ex1e-5 (Fig.2G), suggesting that $10^{-4}m^2$ is likely too large of a background mixing value. In Ex1e-5, the mean annual cumulative net flux of carbon into the ocean, integrated from 75°S northward to 30°S, is 1 Pg C/yr (Fig.2D). In Ex1e-4 only 0.6 Pg C/yr is taken up, a reduction of 0.4 Pg C yr⁻¹. The annual uptake of ExVar falls between the other two experiments at around 0.8 Pg C/yr. These numbers are for the six-year mean, and as panel B shows, the reductions from Ex1e-5 are much higher over the first three years (almost double).

The cumulative carbon fluxes are compared to other estimates of the integrated SO carbon flux from 75°S northward to up to 45°S and 35°S for the period 2015-2017 (Fig.2D; Bushinsky et al. (2019); Landschützer et al. (2016); Rödenbeck et al. (2013)). At 45°S, the Ex1e-5 cumulative flux lies between the three observationally inferred estimates, while the ExVar flux is slightly lower, with Ex1e-4 being the lowest of all three, well below the estimates of the other studies. At 35°S, there is a larger range in carbon uptake between the three model runs. Ex1e-5 is the only experiment that lies within the bounds of the three observational estimates, though it appears towards the lower end, whilst ExVar and Ex1e-4 are below. This further suggests that the lower mixing in Ex1e-5 could be a more suitable background mixing value.

Changes to surface ocean pCO_2

Given that ExVar estimates of carbon fluxes fall between those of Ex1e-4 and Ex1e-5, hereafter, we only focus on the differences between Ex1e-4 and Ex1e-5. Air-sea carbon fluxes exist due to the difference in pCO_2 between the atmosphere and the surface ocean. The high (low) surface ocean pCO_2 values result in regions of low (high) oceanic uptake or even outgassing of CO_2 from the atmosphere (Fig.3A). A region of exception is under sea ice, where the diffusive flux of gases is prevented. The changes in carbon fluxes due to altered mixing, as in figure 2, are due to changes in surface ocean pCO_2 , as atmospheric conditions are constant across experiments.

The annual mean pCO_2 of the surface ocean is higher in Ex1e-4 than in Ex1e-5 in almost all regions, reducing the pCO_2 gradient and carbon uptake (Fig.3B). The areas of greatest increase in pCO_2 include south of South Africa and the waters east of the West Antarctic Peninsula. Small regions where the annual mean pCO_2 is reduced in Ex1e-4 include latitudes of around 30°S, especially to the east of Australia, the Argentine basin, and a few small bands just off the coast of Antarctica in the south.

Using the methodology set out by Takahashi et al. (2014), we break down the pCO_2 change to contributions from changes in the upper ocean content of salinity, temperature, DIC and alkalinity (equation 1). The change in pCO_2 as a contribution from each of the four tracers is calculated using equations 2-5, where $\bar{p}CO_2$ is the mean pCO_2 , \bar{Alk} is the mean alkalinity, γ_{CO_2} is the Revelle factor for CO_2 (value used = 11), and γ_{ALK} is the Revelle factor for alkalinity (value used = -10).

$$\begin{aligned}
\Delta pCO_2 &= \left(\frac{\delta pCO_2}{\delta T}\right)\Delta T + \left(\frac{\delta pCO_2}{\delta DIC}\right)\Delta DIC + \left(\frac{\delta pCO_2}{\delta Alk}\right)\Delta Alk + \left(\frac{\delta pCO_2}{\delta S}\right)\Delta S \quad (1) \\
\frac{\delta pCO_2}{\delta T}\Delta T &= 2(pCO_2)[Exp(0.0423(\pm 0.0002)\Delta T/2) - 1] \quad (2) \\
\left(\frac{\delta pCO_2}{\delta DIC}\right) &= \gamma_{CO_2}(\bar{p}CO_2/\bar{T}CO_2) \quad (3) \\
\frac{\delta pCO_2}{\delta Alk} &= \gamma_{ALK}(\frac{\bar{p}CO_2}{\bar{Alk}}) \quad (4) \\
\left(\frac{\delta pCO_2}{\delta S}\right) &= 0.026(\pm 0.002) \cdot \bar{p}CO_2 \quad (5)
\end{aligned}$$

The four individual contributions, shown in Fig.3D-G, can be summed together to give the annual mean approximated change in pCO_2 (Fig.3C). This calculated change agrees satisfactorily with the changes in pCO_2 between the two experiments (Fig.3B). This verifies the assumptions made in equations 2-5, and confirms that changes to the distribution of these tracers are key in causing changes to carbon fluxes (Fig.3B,C). The only region where the Takahashi et al. method does not capture the changes is in the north of the SO, west of New Zealand and east of South America in the Argentine basin. This is likely due to enhanced water mass mixing occurring in these regions, making changes in this area complex to approximate with simple assumptions. While the calculations shown in Fig. 3 use the upper 2.6 m of the water column, they are not sensitive to depth and similar results are found down to ~ 55 m.

On an annual basis, contributions from changes in DIC and alkalinity concentrations are the main drivers of changes in pCO_2 , with the contributions from salinity and temperature being secondary (Fig.3E,F). An increase in the alkalinity content decreases pCO_2 , whilst an increase in salinity or DIC increases pCO_2 . Where the temperature increases, pCO_2 increases due to modulation of the equilibrium DIC. The increase in the DIC content of the surface waters of the southern SO in Ex1e-4 increases pCO_2 , whilst in the north the decrease in DIC concentration decreases pCO_2 . On the contrary, the increase in alkalinity concentration in the south decreases pCO_2 , while the decrease in alkalinity in the north increases pCO_2 . Changes in salinity concentrations act to slightly increase the pCO_2 in Ex1e-4. Temperature changes with enhanced mixing cause a slight decrease in pCO_2 in the north and an increase in pCO_2 in the south in Ex1e-4.

Changes in the upper ocean temperature, salinity, DIC and alkalinity are due to alterations to the diapycnal flux of these tracers. The diapycnal flux for a tracer with concentration C may be approximated by $-K_v \times \frac{\partial C}{\partial z}$. Therefore, if vertical diapycnal mixing K_v is increased, more tracer, e.g. DIC, is mixed downgradient (upward into the surface waters). This increase in upward flux is the strongest where the vertical gradients are the strongest. Therefore, strong correlations develop between locations with sharp vertical gradients and locations with significantly altered tracer content with enhanced mixing (Fig.4A-D). This correlation is especially clear when examining changes to tracer distributions in the first month of the perturbation experiments, as shown in figure 4.

Regions that experience high changes in DIC concentration with enhanced mixing are around the coast of Antarctica, south of $60^\circ S$ and above depths of 40 m. In these areas, surface waters are fed by wind-induced upwelling of deep waters rich in DIC due to the respiration of organic material. Further to the north, the upper 120 m of the water column has weak vertical gradients of DIC concentration (Fig.4E,F). The dipole pattern shown when looking in a zonal average sense implies the erosion of the sharp gradient by enhanced mixing. The DIC concentration increases with increased mixing in the upper surface waters (shown in red), while concentrations decrease between 40m and 20m depth (shown in blue) due to a flux divergence, as more of this carbon has been mixed upwards into the surface waters (Fig.4G). There is a clear divide at around 20 m; this depth corresponds to the depth of the maximum vertical gradient. Changes in alkalinity and salinity roughly follow

a pattern similar to DIC (hence not shown). The greatest changes in temperature occur in different regions, mainly in the northern SO, especially at around 90°E, in the Argentine basin, and in the waters surrounding New Zealand.

Temporal and seasonal variability of changes in $p\text{CO}_2$

Carbon fluxes show strong seasonal and spatial variations (Fig.5), as for example, discussed in Rosso et al. (2017). In the austral summer (December to February), the SO from 60°S to 30°S is a net source of CO_2 outgassing (Fig.5A,B Dashed lines). Some outgassing also occurs at the upwelling zone of the polar front, especially in the Atlantic basin (Fig.5C). South of ~60°S, the SO acts as a slight carbon sink even in summer. Austral winter (June to August) has much higher carbon uptake than summer, with the net uptake occurring in almost all regions of the SO, except beneath sea ice (Fig.5A,B,D). Small outgassing regions exist around the polar front and at the upwelling region off the west coast of South America in the Argentine basin (Fig.5D).

While figures 2 and 3 show the changes to carbon fluxes between model runs in an annual mean sense, there are also significant temporal patterns in how mixing perturbation alters carbon fluxes (as will be discussed in Fig.8). Figures 5 and 6 examine the dominant mechanisms for seasonal differences observed in the changes to $p\text{CO}_2$ between Ex1e-4, ExVar and Ex1e-5. The changes in carbon fluxes between experiments are greater in winter than in summer (Fig.5A,E,F). An exception is in the very south, where ice cover during winter reduces gas exchange in all experiments. In winter, Ex1e-4 has a reduced carbon uptake compared to Ex1e-5, while ExVar has a similar carbon uptake to Ex1e-5 (Fig.5A). Cumulatively integrated winter carbon fluxes are reduced from almost 2 Pg C/yr in Ex1e-5 to 1.2 Pg C/yr in Ex1e-4. The greatest decreases in uptake occur around 40°S. The Argentine basin is also a region of pronounced diminished carbon uptake (Fig.5F). Three small areas on the edge of the winter ice extent experience increased carbon uptake in the winter due to reduced ice cover, the reason for which is explained subsequently (Blue areas, Fig.5F). Summer changes to carbon fluxes are of a smaller magnitude and show more spatial variability than the winter months (Fig.5A,E). In summer, the cumulative integrated outgassing of Ex1e-5 is higher than Ex1e-4, and ExVar is higher than both Ex1e-4 and Ex1e-5, though the difference between all three runs is less than 0.2 Pg C/yr. At lower latitudes where the SO is a net source of carbon to the atmosphere, outgassing is decreased in Ex1e-4. Further south, where the SO is a carbon sink, CO_2 uptake is reduced in Ex1e-4 (Fig.5E). Changes in flux occur as far south as the Antarctic continent due to diminished summer sea ice.

Using Eqs.1-5 and Fig. 3, we next use the Takahashi *et al.* methodology to examine seasonal changes to tracer contributions and their implications for the $p\text{CO}_2$ and carbon fluxes. The outcome is shown in Fig. 6. Salinity contributions to changes to $p\text{CO}_2$ are not shown as they are negligible compared to DIC, alkalinity, and temperature contributions. The temperature contribution varies greatly between seasons, being stronger in January than in July (Fig.6B,E). Closer to Antarctica, changes in temperature increase the $p\text{CO}_2$ of Ex1e-4 surface waters throughout the year. In July, this positive contribution extends further north. In January, the change in temperature causes very strong reductions in $p\text{CO}_2$, especially in the subtropical gyres. Because the change in surface temperature and associated change to $p\text{CO}_2$ vary with season, the annual mean change in temperature and its contribution to change in $p\text{CO}_2$ appear much smaller (Fig.3D). They are nevertheless key to driving the seasonal response of changing SO carbon fluxes in response to altered diapycnal mixing.

The vertical structure of the thermocline and the associated change in surface temperature with enhanced mixing have seasonal trends (Fig.7B,F). In January, surface waters are warm, and the temperature declines rapidly with depth down to 100 m, especially north of 60°S (Fig.7A). South of 60°S and below 100 m, water temperature increases with depth due to the upwelling of deep warm waters of North-Atlantic origin through Ekman transport.

In Ex1e-4, subsurface cooler waters are mixed more strongly towards the surface, cooling the surface waters and warming the subsurface waters relative to Ex1e-5 (Fig.7B). This surface cooling reduces the $p\text{CO}_2$ (Fig.6A). In July the surface waters are well mixed and there is no temperature gradient in the upper 100 m (Fig.7E). Below the winter mixed layer, temperature rises with depth. Enhanced mixing warms surface waters, increasing the $p\text{CO}_2$ (Fig.6E,F). This increase in surface temperature also increases the rate of sea ice melt, reducing the sea ice cover toward the end of winter/ spring in Ex1e-4. This results in small regions of increased carbon uptake around the sea ice edge in winter (Fig.5F). North of 60°S and below the mixed layer, waters still decrease in temperature with depth, so increased mixing cools the surface waters (Fig.7E,F). The vertical gradients of DIC and alkalinity are relatively constant regardless of season (Fig.7C,G). Changes in DIC and alkalinity concentrations have opposing effects on $p\text{CO}_2$ (Fig.3E,F), but together act to increase $p\text{CO}_2$ at all latitudes in summer and winter in Ex1e-4 (Fig.6C,F). The increase to $p\text{CO}_2$ in Ex1e-4 from combined carbonate chemistry changes is stronger in the winter than in summer, especially north of 40°S (Fig.6C,F).

Though all six years of the model run exhibit a similar seasonal cycle of changes to carbon fluxes with enhanced mixing in Ex1e-4, important inter-annual differences exist (Fig.8) which would not be appreciated in annual and seasonal means. Some differences in carbon fluxes between the two experiments become more pronounced over time, while other changes become less. North of 40°S , Ex1e-4 has an increase in carbon uptake (or reduced outgassing) during the summer. This becomes more pronounced and extends further south down to 50°S in subsequent summers as the model run progresses. While the winter time reductions in uptake in Ex1e-4 compared to Ex1e-5 around 45°S become stronger through the six years, the reductions in carbon uptake south of 60°S become weaker. The SO yearly mean change in C flux (red stars, Fig.8B) show a smaller mean change in the carbon flux between Ex1e-4 and Ex1e-5 in the later years of the run compared to earlier years. This is due to opposing signs of change to carbon fluxes over the seasons becoming more pronounced and therefore causing an antagonistic net effect to changes in an annual mean sense.

40°S approximately corresponds to the mean latitude of the subtropical front (STF) and marks a regime in terms of the leading mechanisms responsible for changes in $p\text{CO}_2$ and carbon fluxes. This marks the boundary between the nutrient deplete sub-tropical waters to the north and the nutrient and DIC rich waters to the south (Chapman et al., 2020). Regions to the north of this divide are responsible for the summer increases in carbon uptake in Ex1e-4 in later years of the run. In contrast, regions to the south are responsible for the strong response of reduced carbon uptake in Ex1e-4.

The contributions to the total change in $p\text{CO}_2$ are drastically different across the STF (Fig.8C-E). To its South, opposite changes in $p\text{CO}_2$ due to alkalinity and DIC nearly balance, with the latter being slightly larger (Fig.8D). As before, salinity contributions remain negligible at all times. Over the first two years of the perturbation, the total change in $p\text{CO}_2$ is positive, meaning $p\text{CO}_2$ is higher in Ex1e-4 than in Ex1e-5. The magnitude of the reduction in $p\text{CO}_2$ due to Alkalinity increases over time. The magnitude of total $p\text{CO}_2$ change decreases over time and becomes negative in the summer months, allowing for increased carbon uptake.

North of the STF, DIC and alkalinity do not balance each other out (Fig.8E) and changes in temperature between the two model runs are more dominant. Alkalinity increases $p\text{CO}_2$ north of the STF, while changes in DIC initially also increase the $p\text{CO}_2$ in Ex1e-4. By the summer of the third year of the run, changes in DIC begin to reduce the $p\text{CO}_2$, causing the net total change in $p\text{CO}_2$ to be negative in summer. This causes an increase in carbon uptake in the summer north of the STF in Ex1e-4.

Almost all changes in DIC between Ex1e-4 and Ex1e-5 are due to altered diapycnal fluxes of DIC. However, north of the STF, DIC contribution to decreased $p\text{CO}_2$ in the summer is due to increased productivity in the nutrient depleted waters of the sub tropical

gyre. This increase in productivity does not occur instantaneously, but instead takes around 6 months to begin decreasing the DIC contribution (red line, Fig.8E and Fig.9C). While an increase in productivity occurs with higher mixing across the whole SO region, it is only in the north, roughly north of the sub tropical front where increased phytoplankton production and DIC uptake becomes the dominant mechanism in altering DIC concentrations. Thus, in the context of this paper, we consider the STF as the upper boundary of the SO and postpone further discussion on the biologically-dominated change in $p\text{CO}_2$ north of the SO to future work.

Comparison to $p\text{CO}_2$ observational data

The $p\text{CO}_2$ values for Ex1e-4, Ex1e-5 and ExVar can be compared to 2013-2018 observed levels from the Surface Ocean CO_2 Atlas (SOCAT) (Bakker et al., 2016) (Fig.10). Neither clearly matches SOCAT observations better than the other (Fig.10A). Regional trends are also unclear, although from the limited data available, Ex1e-5 appears to better represent the $p\text{CO}_2$ of the northern Pacific Ocean, as well as off the coast of South Africa and Tasmania. Meanwhile estimates from Ex1e-4 are better matched to observations in the western Atlantic and the northern Indian Oceans.

The probability density function for the difference between SOCAT and B-SOSE for the three experiments is broken down over seasons (Fig.10B). In summer the standard deviation of differences between ExVar and data is much larger than those for Ex1e-4 and Ex1e-5. The mean difference of $15.5 \mu\text{atm}$ for Ex1e-5 is lower than $17.46 \mu\text{atm}$ for Ex1e-4, whilst ExVar has the lowest mean difference from observations. The high-end tails of the distributions are more skewed than the lower ends, implying a systematic over-estimate of $p\text{CO}_2$ by B-SOSE. B-SOSE overestimates the flux of carbon from the ocean to the atmosphere or underestimates the SO carbon uptake from the atmosphere, particularly in the summer.

SOCAT data is heavily biased towards summer data due to limitations on data collection in the winter. The mean difference between SOCAT and B-SOSE is lower for the winter mean than for the summer in all experiments. In the winter, ExVar has the largest mean difference from observations but also the largest standard deviation. In an annual mean sense, ExVar does a better job in matching SOCAT observations, though with a much higher standard deviation. It is interesting to note that, while in the annual mean sense, ExVar better matches SOCAT observations of $p\text{CO}_2$, Ex1e-5 was better able to replicate previous observational estimates of cumulative SO C fluxes (Fig.2D).

Conclusion

We have demonstrated that the air-sea carbon fluxes in the SO are highly sensitive to modest background mixing variations well within the range of our best estimates. This is despite background mixing rates being orders of magnitude smaller than mixed layer model generated mixing. We find that the overall changes to carbon fluxes depend on the interactive effects of changes to DIC, temperature, and alkalinity, which can compensate or reinforce each other, and the predominant driver varies regionally, seasonally and temporally as additive and opposing feedbacks kick in at varying time scales.

The relevance of diapycnal mixing in setting global carbon fluxes has previously been considered to be through changes to the underlying stratification and of regional and global overturning circulation and ventilation patterns. Although that may be true on centennial or longer timescales, here we show that on much faster timescales mixing directly acts upon tracers such as DIC, alkalinity, temperature, and salinity leading to a significant change in surface ocean carbon fluxes.

The high correlation found between vertical gradients and strong changes in tracer distributions with altered mixing shows that on a timescale of days to months, direct changes

in diapycnal mixing fluxes are the predominant drivers of the $p\text{CO}_2$ response in the SO. On longer timescales, from months to years, further feedbacks involving changes to biological productivity and mixed layer depth will also begin to cause further changes to the surface ocean $p\text{CO}_2$. A latitudinal divide exists at around 40°S , roughly the location of the subtropical front. High vertical tracer gradients cause the direct impact of altered tracer fluxes to dominate trends to the south, whilst changes in biological productivity play a key role in the observed changes to carbon fluxes to the north.

Two major issues stand in the way of better constraining of the data-assimilating ocean estimates insofar as the role of vertical mixing in the upper ocean is concerned. First, despite the significant investments in observations such as SOCAT, Fig. 10A clearly shows the sparsity of the available observational data. From a statistical perspective, this coverage is insufficient to discern which background mixing value better represents the real ocean despite the strong impact of these choices on $p\text{CO}_2$. This issue can be resolved only through sustained observations. Knowledge of the seasonal cycle of $p\text{CO}_2$ is worse in the SO than in most other regions of the ocean. The strong seasonality of the sensitivity of carbon fluxes to altered mixing demonstrates the importance of year-round observations. Second, SO diapycnal mixing can vary by orders of magnitude over timescales ranging from hourly to seasonally, as well as varying spatially. To achieve a close agreement with observations, a model should have a representation of such variability. ExVar employed our best estimate of a time-mean spatially variable mixing map, resulting in carbon fluxes similar to that obtained with a constant diffusivity of $10^{-5}\text{m}^2/\text{s}$. Direct observations of diapycnal mixing in the SO have suggested that such maps (a) lack the representation of many key processes that result in higher turbulence in upper surface waters (e.g. bottom-generated lee waves, shoaling of remotely generated internal tides) and (b) do not allow for co-variance of mixing and tracer gradients, key to biological processes. This work highlights the absolute necessity for climate models to resolve the spatio-temporal variability of small-scale turbulent mixing, or to skillfully parameterise the processes responsible for generating them.

1 Data and material availability

The data sets generated during and/or analysed during the current study are available from the corresponding author on reasonable request and from <http://sose.ucsd.edu>.

The data used to construct the spatially variable mixing map used for ExVar is available at <https://agupubs.onlinelibrary.wiley.com/doi/full/10.1029/2020MS002065>.

References

- Adkins, J. F. (2013, 9). The role of deep ocean circulation in setting glacial climates. *Paleoceanography*, 28(3), 539–561. Retrieved from <http://doi.wiley.com/10.1002/palo.20046> doi: 10.1002/palo.20046
- Alford, M. H. (2020). Global calculations of local and remote near-inertial-wave dissipation. *Journal of Physical Oceanography*, 50(11), 3157–3164.
- Arias, P., Bellouin, N., Coppola, E., Jones, R., Krinner, G., Marotzke, J., ... others (2021). Climate change 2021: The physical science basis. contribution of working group 14 i to the sixth assessment report of the intergovernmental panel on climate change; technical summary.
- Baker, L., & Mashayek, A. (2021). Surface reflection of bottom generated oceanic lee waves. *Journal of Fluid Mechanics*, 924, A17.
- Baker, L., & Mashayek, A. (2022). The impact of realistic topographic representation on the parameterisation of oceanic lee wave energy flux. *Authorea Preprints*.
- Bakker, D. C., Pfeil, B., Landa, C. S., Metzl, N., O'Brien, K. M., Olsen, A., ... Xu, S. (2016, sep). *A multi-decade record of high-quality $f\text{CO}_2$ data in version 3 of the Surface Ocean CO_2 Atlas (SOCAT)* (Vol. 8) (No. 2). Retrieved from <https://essd.copernicus.org/articles/8/383/2016/> doi: 10.5194/essd-8-383-2016

- Bianchi, D., Galbraith, E. D., Carozza, D. A., Mislan, K., & Stock, C. A. (2013). Intensification of open-ocean oxygen depletion by vertically migrating animals. *Nature Geoscience*, 6(7), 545–548.
- Bushinsky, S. M., Landschützer, P., Rödenbeck, C., Gray, A. R., Baker, D., Mazloff, M. R., ... Sarmiento, J. L. (2019, 11). Reassessing Southern Ocean Air-Sea CO₂ Flux Estimates With the Addition of Biogeochemical Float Observations. *Global Biogeochemical Cycles*, 33(11), 1370–1388. Retrieved from <https://onlinelibrary.wiley.com/doi/abs/10.1029/2019GB006176> doi: 10.1029/2019GB006176
- Cael, B., & Mashayek, A. (2021). Log-skew-normality of ocean turbulence. *Physical Review Letters*, 126(22), 224502.
- Chapman, C. C., Lea, M. A., Meyer, A., Sallée, J. B., & Hindell, M. (2020). Defining Southern Ocean fronts and their influence on biological and physical processes in a changing climate. *Nature Climate Change*. doi: 10.1038/s41558-020-0705-4
- Dee, D. P., Uppala, S. M., Simmons, A. J., Berrisford, P., Poli, P., Kobayashi, S., ... others (2011). The era-interim reanalysis: Configuration and performance of the data assimilation system. *Quarterly Journal of the royal meteorological society*, 137(656), 553–597.
- de Lavergne, C., Vic, C., Madec, G., Roquet, F., Waterhouse, A. F., Whalen, C. B., ... Hibiya, T. (2020, 5). A Parameterization of Local and Remote Tidal Mixing. *Journal of Advances in Modeling Earth Systems*, 12(5), e2020MS002065. Retrieved from <https://onlinelibrary.wiley.com/doi/abs/10.1029/2020MS002065> doi: 10.1029/2020MS002065
- DeVries, T., & Primeau, F. (2011, 12). Dynamically and Observationally Constrained Estimates of Water-Mass Distributions and Ages in the Global Ocean. *Journal of Physical Oceanography*, 41(12), 2381–2401. Retrieved from <https://journals.ametsoc.org/jpo/article/41/12/2381/11258/Dynamically-and-Observationally-Constrained> doi: 10.1175/JPO-D-10-05011.1
- Dunne, J. P., Armstrong, R. A., Gnanadesikan, A., & Sarmiento, J. L. (2005). Empirical and mechanistic models for the particle export ratio. *Global Biogeochemical Cycles*, 19(4).
- Dutkiewicz, S., Follows, M. J., Heimbach, P., & Marshall, J. (2006). Controls on ocean productivity and air-sea carbon flux: An adjoint model sensitivity study. *Geophysical Research Letters*, 33(2).
- Dutreuil, S., Bopp, L., & Tagliabue, A. (2009). Impact of enhanced vertical mixing on marine biogeochemistry: Lessons for geo-engineering and natural variability. *Biogeosciences*, 6(5), 901–912. Retrieved from www.biogeosciences.net/6/901/2009/ doi: 10.5194/bg-6-901-2009
- Ellison, E., Mashayekh, A., & Cimolo, L. (2021). Multi-timescale control of southern ocean diapycnal mixing over atlantic tracer budgets.
- Fenty, I., & Heimbach, P. (2013). Coupled sea ice–ocean-state estimation in the labrador sea and baffin bay. *Journal of physical oceanography*, 43(5), 884–904.
- Ferrari, R. (2014). *Oceanography: What goes down must come up*. doi: 10.1038/513179a
- Follows, M. J., Ito, T., & Dutkiewicz, S. (2006, jan). On the solution of the carbonate chemistry system in ocean biogeochemistry models. *Ocean Modelling*, 12(3-4), 290–301. Retrieved from <https://www.sciencedirect.com/science/article/abs/pii/S1463500305000533> doi: 10.1016/J.OCEMOD.2005.05.004
- Galbraith, E. D., Dunne, J. P., Gnanadesikan, A., Slater, R. D., Sarmiento, J. L., Dufour, C. O., ... others (2015). Complex functionality with minimal computation: Promise and pitfalls of reduced-tracer ocean biogeochemistry models. *Journal of Advances in Modeling Earth Systems*, 7(4), 2012–2028.
- Galbraith, E. D., Gnanadesikan, A., Dunne, J. P., & Hiscock, M. R. (2010). Regional impacts of iron-light colimitation in a global biogeochemical model. *Biogeosciences*, 7(3), 1043–1064.
- Ganachaud, A., & Wunsch, C. (2000). Improved estimates of global ocean circulation, heat

- transport and mixing from hydrographic data. *Nature*, 408(6811), 453–457.
- Garabato, A. C. N., Frajka-Williams, E. E., Spingys, C. P., Legg, S., Polzin, K. L., Forryan, A., ... others (2019). Rapid mixing and exchange of deep-ocean waters in an abyssal boundary current. *Proceedings of the National Academy of Sciences*, 116(27), 13233–13238.
- Garabato, A. C. N., Polzin, K. L., King, B. A., Heywood, K. J., & Visbeck, M. (2004). Widespread intense turbulent mixing in the southern ocean. *Science*, 303(5655), 210–213.
- Garcia, H. E., Locarnini, R. A., Boyer, T. P., Antonov, J. I., Baranova, O. K., Zweng, M. M., ... Levitus, S. (2013). World ocean atlas 2013. volume 4, dissolved inorganic nutrients (phosphate, nitrate, silicate).
- Gaspar, P., Grégoris, Y., & Lefevre, J.-M. (1990). A simple eddy kinetic energy model for simulations of the oceanic vertical mixing: Tests at station papa and long-term upper ocean study site. *Journal of Geophysical Research: Oceans*, 95(C9), 16179–16193.
- Gaspar, P., Grégoris, Y., & Lefevre, J.-M. (1990, sep). A simple eddy kinetic energy model for simulations of the oceanic vertical mixing: Tests at station Papa and long-term upper ocean study site. *Journal of Geophysical Research*, 95(C9), 16179. Retrieved from <http://doi.wiley.com/10.1029/JC095iC09p16179> doi: 10.1029/JC095iC09p16179
- Gruber, N., Landschützer, P., & Lovenduski, N. S. (2019). The variable southern ocean carbon sink. *Annual review of marine science*, 11, 159–186.
- Klocker, A. (2018). Opening the window to the Southern Ocean: The role of jet dynamics. *Science Advances*. doi: 10.1126/sciadv.aao4719
- Landschützer, P., Gruber, N., & Bakker, D. C. E. (2016, 10). Decadal variations and trends of the global ocean carbon sink. *Global Biogeochemical Cycles*, 30(10), 1396–1417. Retrieved from <http://doi.wiley.com/10.1002/2015GB005359> doi: 10.1002/2015GB005359
- Large, W., & Yeager, S. (2009). The global climatology of an interannually varying air–sea flux data set. *Climate dynamics*, 33(2), 341–364.
- Large, W. G., McWilliams, J. C., & Doney, S. C. (1994). Oceanic vertical mixing: A review and a model with a nonlocal boundary layer parameterization. *Reviews of geophysics*, 32(4), 363–403.
- Ledwell, J. R., St. Laurent, L. C., Garton, J. B., & Toole, J. M. (2011). Diapycnal mixing in the antarctic circumpolar current. *Journal of Physical Oceanography*, 41(1), 241–246. Retrieved from <http://www.rocklandscientific.com> doi: 10.1175/2010JPO4557.1
- Losch, M., Menemenlis, D., Campin, J.-M., Heimbach, P., & Hill, C. (2010). On the formulation of sea-ice models. part 1: Effects of different solver implementations and parameterizations. *Ocean Modelling*, 33(1-2), 129–144.
- Lumpkin, R., & Speer, K. (2007). Global ocean meridional overturning. *Journal of Physical Oceanography*, 37(10), 2550–2562.
- Mahadevan, A., Tagliabue, A., Bopp, L., Lenton, A., Mémer, L., & Lévy, M. (2011, 5). Impact of episodic vertical fluxes on sea surface pCO₂. *Philosophical Transactions of the Royal Society A: Mathematical, Physical and Engineering Sciences*, 369(1943), 2009–2025. Retrieved from <https://royalsocietypublishing.org/doi/10.1098/rsta.2010.0340> doi: 10.1098/rsta.2010.0340
- Marinov, I., & Gnanadesikan, A. (2011, 2). Changes in ocean circulation and carbon storage are decoupled from air–sea CO₂ fluxes. *Biogeosciences*, 8(2), 505–513. Retrieved from <https://bg.copernicus.org/articles/8/505/2011/> doi: 10.5194/bg-8-505-2011
- Marinov, I., Gnanadesikan, A., Sarmiento, J. L., Toggweiler, J. R., Follows, M., & Mignone, B. K. (2008). Impact of oceanic circulation on biological carbon storage in the ocean and atmospheric pCO₂. *Global Biogeochemical Cycles*. doi: 10.1029/2007GB002958
- Marshall, J., & Speer, K. (2012). Closure of the meridional overturning circulation through Southern Ocean upwelling. *Nature Geoscience*, 5(3), 171–180. Retrieved from [www](http://www.nature.com)

- .nature.com/naturegeoscience doi: 10.1038/ngeo1391
- Mashayek, A., Ferrari, R., Merrifield, S., Ledwell, J., St Laurent, L., & Garabato, A. (2017). Topographic enhancement of vertical turbulent mixing in the Southern Ocean. *Nature Communications*, 8. doi: 10.1038/ncomms14197
- Mashayek, A., Reynard, N., Zhai, F., Srinivasan, K., Jelley, A., Garabato, A. N., & Caulfield, C.-c. P. (2022). Deep ocean learning of small scale turbulence. *Geophysical Research Letters*, e2022GL098039.
- Melet, A., Hallberg, R., Legg, S., Nikurashin, M., Melet, A., Hallberg, R., ... Nikurashin, M. (2014, 3). Sensitivity of the Ocean State to Lee Wave–Driven Mixing. *Journal of Physical Oceanography*, 44(3), 900–921. Retrieved from <http://journals.ametsoc.org/doi/abs/10.1175/JPO-D-13-072.1> doi: 10.1175/JPO-D-13-072.1
- Melet, A. V., Hallberg, R., & Marshall, D. P. (2022). The role of ocean mixing in the climate system. In *Ocean mixing* (pp. 5–34). Elsevier.
- Munk, W. H. (1966). Abyssal recipes. In *Deep sea research and oceanographic abstracts* (Vol. 13, pp. 707–730).
- Nikurashin, M., & Ferrari, R. (2011). Global energy conversion rate from geostrophic flows into internal lee waves in the deep ocean. *Geophysical Research Letters*, 38(8).
- Nikurashin, M., & Ferrari, R. (2013). Overturning circulation driven by breaking internal waves in the deep ocean. *Geophysical Research Letters*, 40(12), 3133–3137.
- Orsi, A. H., Whitworth, T., & Nowlin, W. D. (1995, may). On the meridional extent and fronts of the Antarctic Circumpolar Current. *Deep Sea Research Part I: Oceanographic Research Papers*, 42(5), 641–673. Retrieved from <https://www.sciencedirect.com/science/article/pii/096706379500021W> doi: 10.1016/0967-0637(95)00021-W
- Peters, W., Jacobson, A. R., Sweeney, C., Andrews, A. E., Conway, T. J., Masarie, K., ... others (2007). An atmospheric perspective on north american carbon dioxide exchange: Carbontracker. *Proceedings of the National Academy of Sciences*, 104(48), 18925–18930.
- Rödenbeck, C., Keeling, R. F., Bakker, D. C., Metzl, N., Olsen, A., Sabine, C., & Heimann, M. (2013). Global surface-ocean p co₂ and sea–air co₂ flux variability from an observation-driven ocean mixed-layer scheme. *Ocean Science*, 9(2), 193–216.
- Rosso, I., Mazloff, M. R., Verdy, A., & Talley, L. D. (2017, sep). Space and time variability of the Southern Ocean carbon budget. *Journal of Geophysical Research: Oceans*, 122(9), 7407–7432. Retrieved from <http://doi.wiley.com/10.1002/2016JC012646> doi: 10.1002/2016JC012646
- Sarmiento, J. L., Gruber, N., Brzezinski, M. A., & Dunne, J. P. (2004). High-latitude controls of thermocline nutrients and low latitude biological productivity. *Nature*. doi: 10.1038/nature02127
- Schmittner, A., Urban, N. M., Keller, K., & Matthews, D. (2009). Using tracer observations to reduce the uncertainty of ocean diapycnal mixing and climate-carbon cycle projections. *Global Biogeochemical Cycles*, 23(4). Retrieved from <http://www.nodc.org> doi: 10.1029/2008GB003421
- Shakespeare, C. J. (2020). Interdependence of internal tide and lee wave generation at abyssal hills: Global calculations. *Journal of Physical Oceanography*, 50(3), 655–677.
- Sigman, D. M., Hain, M. P., & Haug, G. H. (2010). *The polar ocean and glacial cycles in atmospheric CO₂ concentration* (Vol. 466) (No. 7302). doi: 10.1038/nature09149
- Swierczek, S., Mazloff, M. R., Morzfeld, M., & Russell, J. L. (2021, jul). The effect of resolution on vertical heat and carbon transports in a regional ocean circulation model of the argentine basin. *Journal of Geophysical Research: Oceans*, 126(7), e2021JC017235. Retrieved from <https://onlinelibrary.wiley.com/doi/10.1029/2021JC017235> doi: 10.1029/2021jc017235
- Takahashi, T., Sutherland, S. C., Chipman, D. W., Goddard, J. G., & Ho, C. (2014). Climatological distributions of pH, pCO₂, total CO₂, alkalinity, and CaCO₃ saturation in the global surface ocean, and temporal changes at selected locations. *Marine Chemistry*. doi: 10.1016/j.marchem.2014.06.004
- Talley, L. D. (2013). Closure of the global overturning circulation through the Indian,

- 675 Pacific, and southern oceans. *Oceanography*, 26(1), 80–97. Retrieved from [http://](http://dx.doi.org/10.5670/oceanog.2013.07)
676 dx.doi.org/10.5670/oceanog.2013.07 doi: 10.5670/oceanog.2013.07
- 677 Talley, L. D., Feely, R. A., Sloyan, B. M., Wanninkhof, R., Baringer, M. O., Bullister,
678 J. L., ... Zhang, J. Z. (2016, 1). Changes in Ocean Heat, Carbon Content, and
679 Ventilation: A Review of the First Decade of GO-SHIP Global Repeat Hydrography.
680 *Annual Review of Marine Science*, 8, 185–215. Retrieved from www.go-ship.org doi:
681 10.1146/annurev-marine-052915-100829
- 682 Talley, L. D., Reid, J. L., & Robbins, P. E. (2003). Data-based meridional overturning
683 streamfunctions for the global ocean. *Journal of Climate*, 16(19), 3213–3226.
- 684 Tamsitt, V., Abernathey, R. P., Mazloff, M. R., Wang, J., & Talley, L. D. (2018). Transfor-
685 mation of Deep Water Masses Along Lagrangian Upwelling Pathways in the Southern
686 Ocean. *Journal of Geophysical Research: Oceans*. doi: 10.1002/2017JC013409
- 687 Verdy, A., & Mazloff, M. R. (2017). A data assimilating model for estimating Southern
688 Ocean biogeochemistry. *Journal of Geophysical Research: Oceans*, 122(9), 6968–6988.
689 Retrieved from <http://hycom.org> doi: 10.1002/2016JC012650
- 690 Wanninkhof, R. (1992). Relationship between wind speed and gas exchange over the ocean.
691 *Journal of Geophysical Research: Oceans*, 97(C5), 7373–7382.
- 692 Waterhouse, A. F., Mackinnon, J. A., Nash, J. D., Alford, M. H., Kunze, E., Simmons,
693 H. L., ... Lee, C. M. (2014). Global patterns of diapycnal mixing from measurements
694 of the turbulent dissipation rate. *Journal of Physical Oceanography*. doi: 10.1175/
695 JPO-D-13-0104.1
- 696 Watson, A. J., Ledwell, J. R., Messias, M. J., King, B. A., Mackay, N., Meredith, M. P., ...
697 Garabato, A. C. N. (2013). Rapid cross-density ocean mixing at mid-depths in the
698 Drake Passage measured by tracer release. *Nature*, 501(7467), 408–411.
- 699 Watson, A. J., & Naveira Garabato, A. C. (2006). The role of Southern Ocean mixing and
700 upwelling in glacial-interglacial atmospheric CO₂ change. *Tellus, Series B: Chemical*
701 *and Physical Meteorology*, 58(1), 73–87. Retrieved from [https://www.tandfonline](https://www.tandfonline.com/action/journalInformation?journalCode=zclb20)
702 [.com/action/journalInformation?journalCode=zclb20](https://www.tandfonline.com/action/journalInformation?journalCode=zclb20) doi: 10.1111/j.1600-0889
703 .2005.00167.x

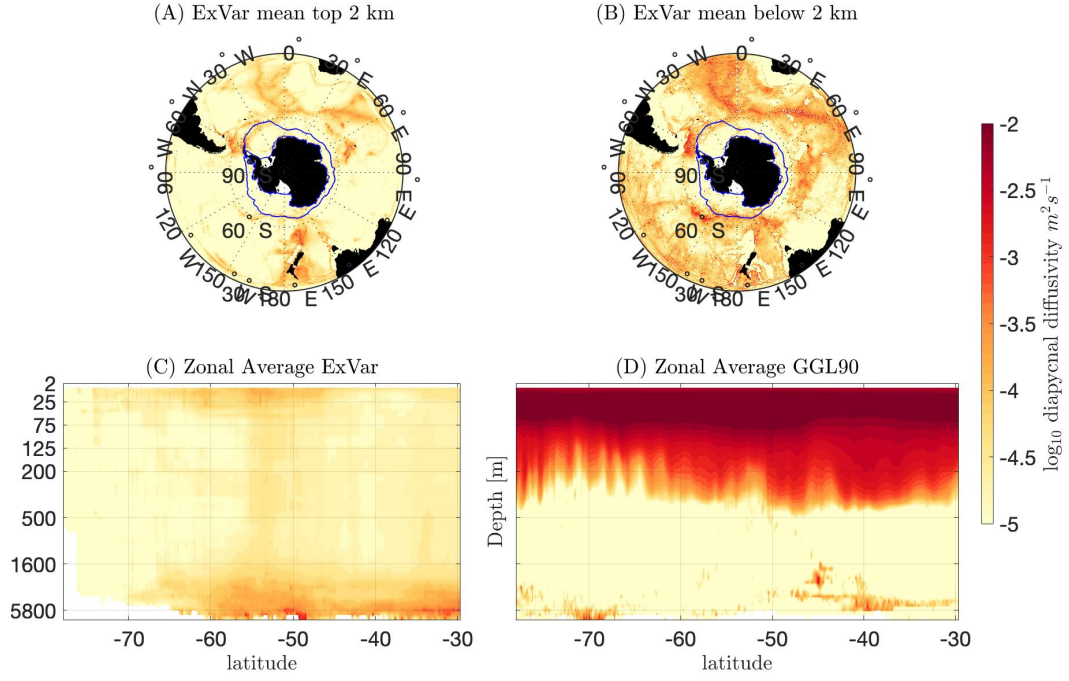


Figure 1: Diapycnal mixing in the Southern Ocean State Estimate (SOSE). The distribution of diapycnal mixing in the Southern ocean, constructed as the sum of contributions from tides and topographically-generated lee waves. This mixing is shown averaged in depth over the top/bottom 2km in panel *A/B*, and zonally over the Southern Ocean in *C*. These maps are used in the spatially variable mixing map experiment (ExVar). For reference, a zonally-averaged map of the storm-induced mixing, as parameterised through GGL90 parameterisation in B-SOSE, is also shown in panel *D*.

704

705

706

707

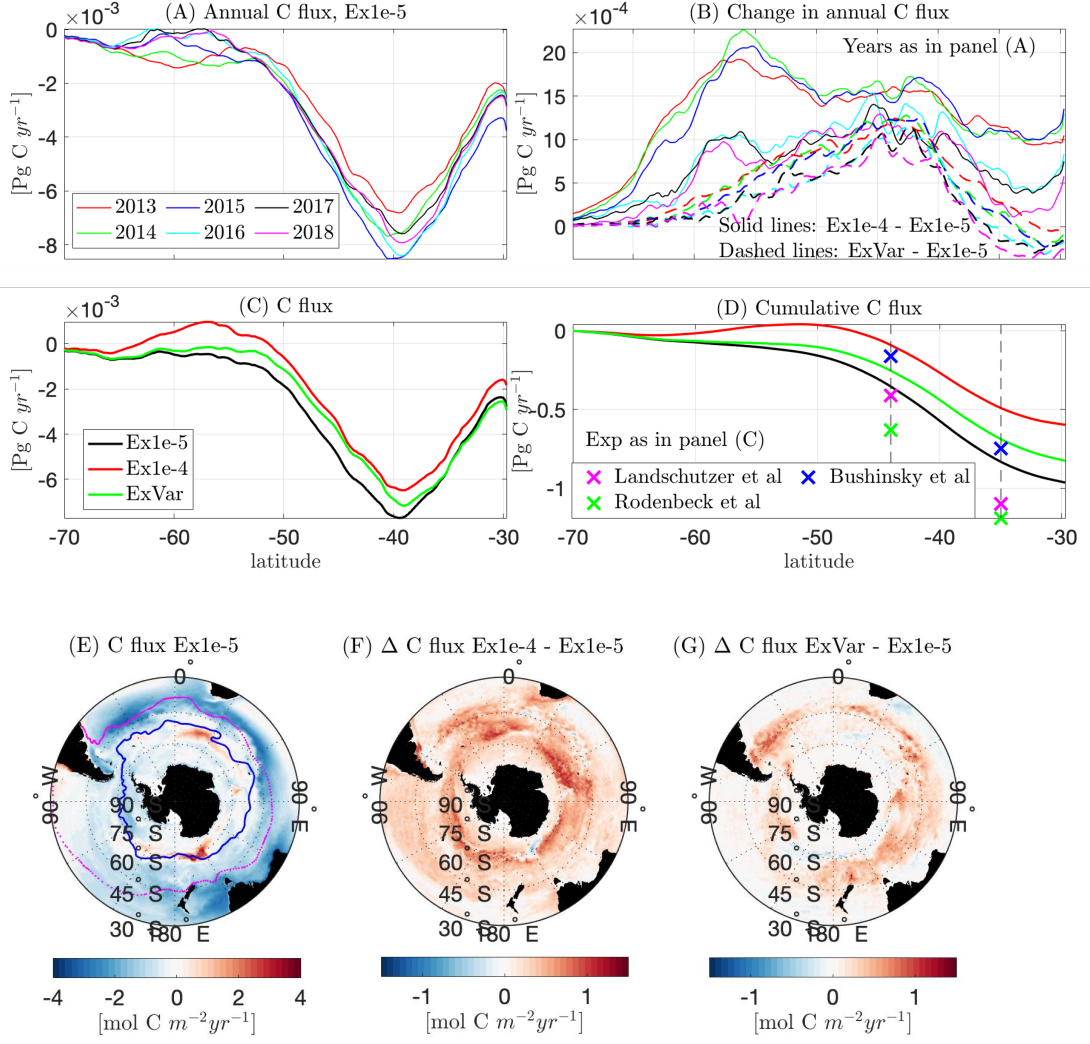


Figure 2: (A) Zonally integrated flux of Carbon for each year of Ex1e-5 (negative = Carbon flux from atmosphere to ocean). (B) Difference in the zonally integrated flux of Carbon between Ex1e-4 and Ex1e-5 (solid lines) and ExVar and Ex1e-5 (dashed lines) for each year of the experiment. (C) zonally integrated annual mean (2013-2018) Carbon flux for Ex1e-4, Ex1e-5 and ExVar. (D) Annual mean (averaged over 2013 to 2018) cumulative integral of carbon fluxes from 70°S northward to 30°S (legend same as the previous panel). Observational markers are included for comparison (Landschützer et al., 2016; Bushinsky et al., 2019; Rödenbeck et al., 2013). (E) Average annual carbon flux for Ex1e-5, the blue line shows the Polar Front, the magenta line shows Sub-tropical Front as defined by Orsi et al. (1995). (F) Annual mean change in Carbon flux (Ex1e-4 – Ex1e-5). (G) Annual mean change in Carbon flux (ExVar – Ex1e-5). Positive values imply reduced carbon uptake or increased outgassing.

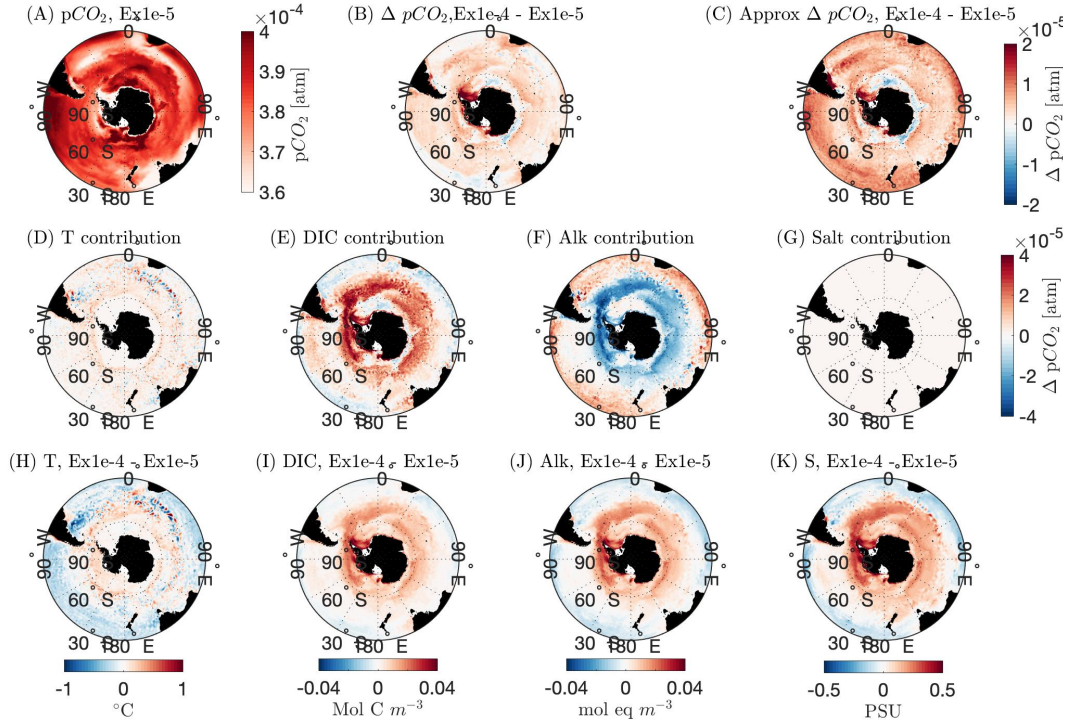


Figure 3: Changes to surface ocean partial pressure and carbon fluxes. (A) Annual mean surface ocean $p\text{CO}_2$ in Ex1e-5. (B) Change in $p\text{CO}_2$ between Ex1e-4 and Ex1e-5. (C) Same as panel B, but this time changes to $p\text{CO}_2$ approximated based on the methodology of Takahashi et al. (2014) that breaks down the change into various contributions as per equations (1-5). The various contributions are shown in panels D-G. (H-K) Changes in annual mean DIC, alkalinity, potential temperature and salinity.

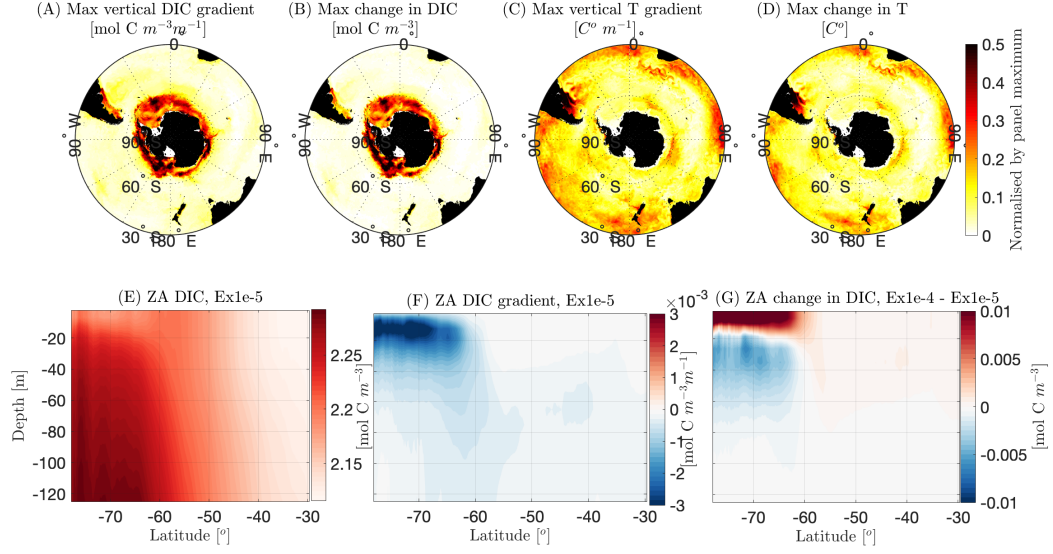


Figure 4: (A) Maximum vertical DIC gradient in the water column for Ex1e-5, normalised by maximum contour value. (B) Maximum change in DIC between Ex1e-4 and Ex1e-5, normalised by the maximum contour value. (C,D) Same as A and B but for temperature. The maximum change in DIC (temperature) is defined as the greatest difference in DIC (temperature) concentration between the two experiments at any depth above 200 m at each latitude and longitude in the domain. (E) Zonal average DIC concentration in Ex1e-5. (F) Zonal average DIC vertical gradient in Ex1e-5; blue indicates a decrease in concentration towards the surface. (G) Zonally averaged change in DIC concentration (Ex1e-4 - Ex1e-5). All shown for December 2012, the first month of all experiments.

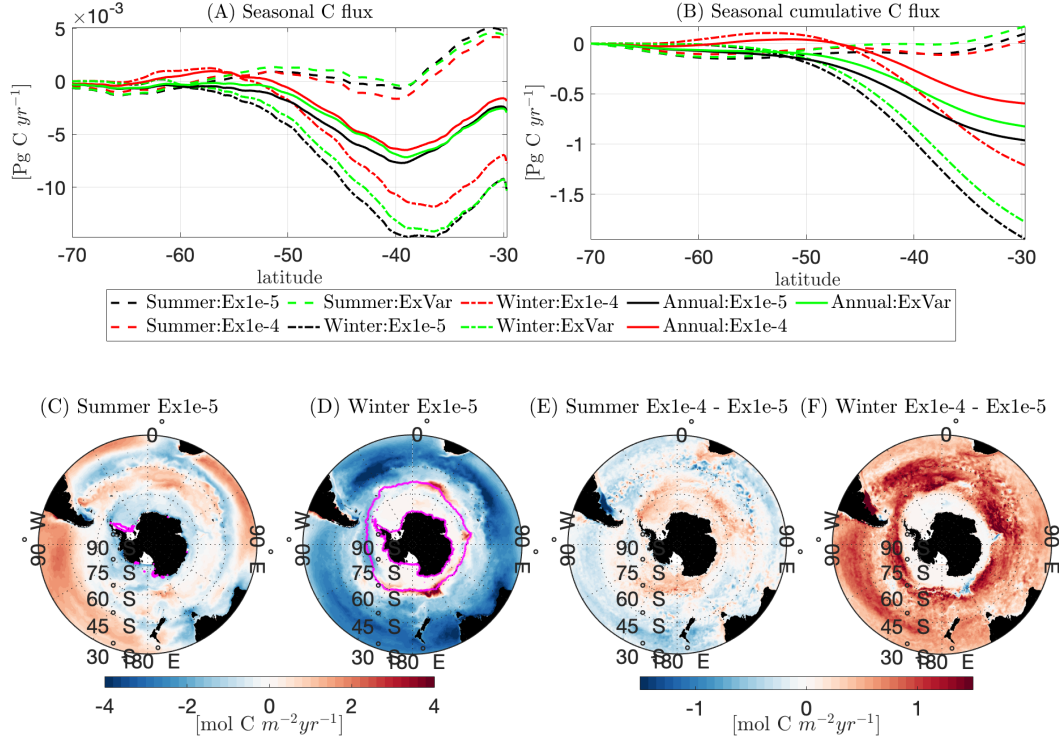


Figure 5: (A) zonally integrated Carbon flux for Ex1e-4, Ex1e-5 and ExVar for summer (dashed), winter (Dotted), and annual mean (solid line). (B) Cumulative sum of carbon fluxes from 70°S northward to 30°S (legend same as the previous panel). (C) Average summer carbon flux for Ex1e-5; magenta lines show the minimum summer ice extent. (D) Average winter carbon flux for Ex1e-5; magenta lines show the maximum winter ice extent. (E) Mean change in summer Carbon flux (Ex1e-4 - Ex1e-5). (F) Mean change in winter Carbon flux (Ex1e-4 - Ex1e-5). Positive values imply reduced carbon uptake or increased outgassing.

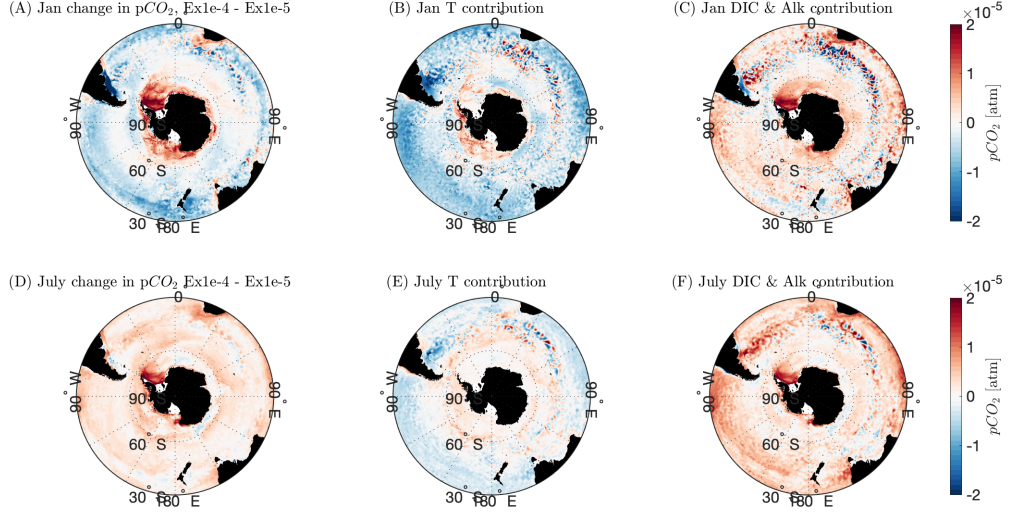


Figure 6: (A) January (summer) 2013-2018 mean change in $p\text{CO}_2$ (Ex1e-4 - Ex1e-5) approximated by the method of Takahashi et al. (2014). (B) Contribution due to changes in temperature. (C) Contribution due to changes in carbon chemistry (DIC and Alkalinity). (D-F) Same as A-C but for July (winter) mean.

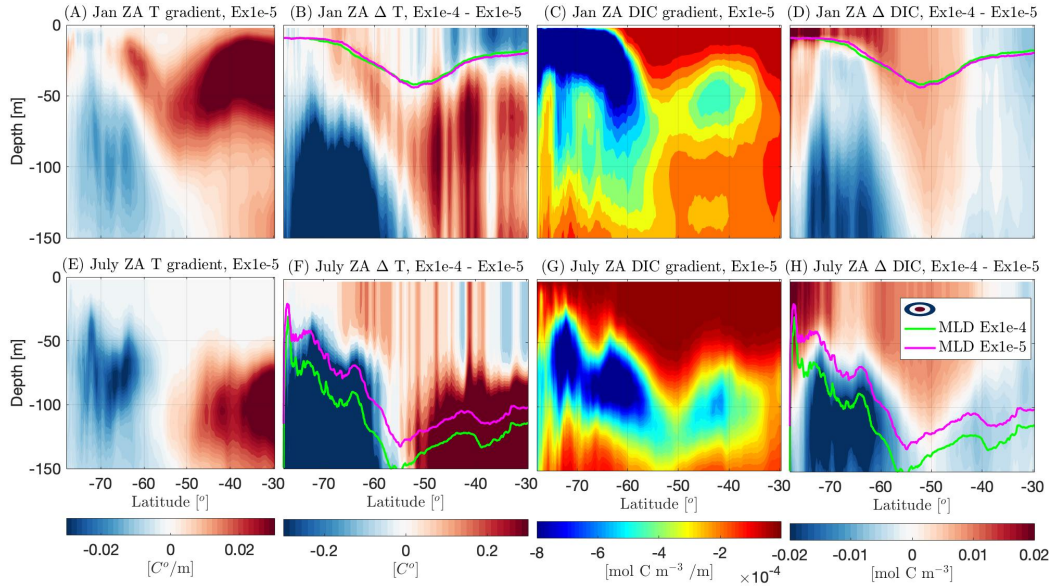


Figure 7: (A) January zonally averaged temperature vertical gradient (red implies increase in temperature towards the surface). (B) January change in temperature (Ex1e-4 - Ex1e-5). Mixed layer depth (MLD) for Ex1e-5 (pink) and Ex1e-4 (green) overlain. (C) January zonally averaged DIC vertical gradient. (D) Change in DIC concentration (Ex1e-4 - Ex1e-5). (E-H) As in A-D but for July mean.

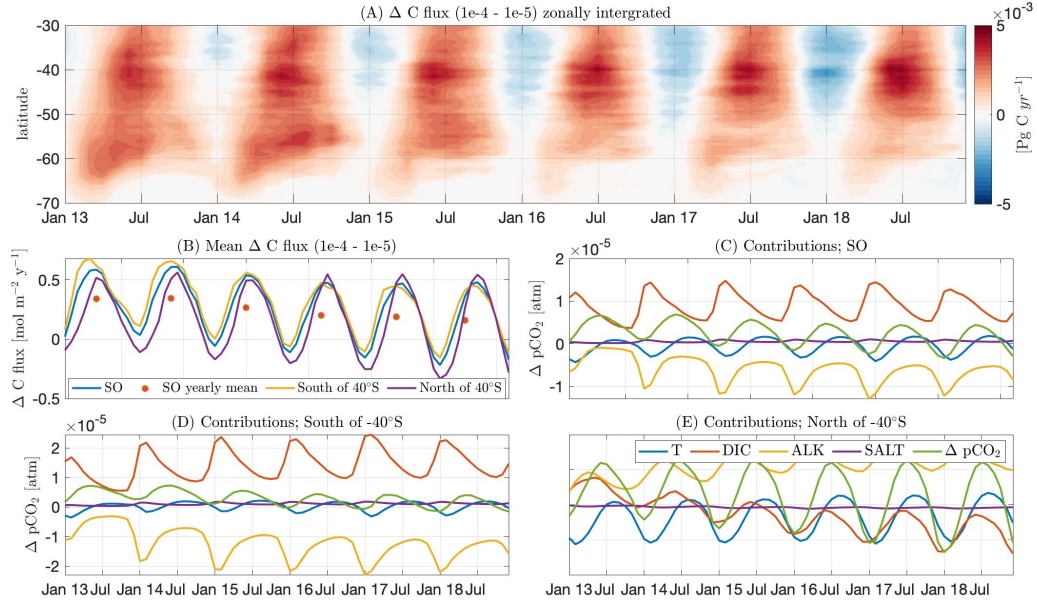


Figure 8: (A) Change in zonally integrated Carbon flux between Ex1e-4 and Ex1e-5 over the six-year time period of Jan 2013 to Dec 2018 (Red shows reduced uptake or increased outgassing in Ex1e-4). (B) Change in the mean carbon flux across the whole SO (blue), the SO North of 40°S (purple) and South of 40°S (yellow) for the same time period. The annual mean change for the whole SO for each year is shown (red star). Using the methodology of Takahashi et al. (2014) as discussed previously, the differences in Carbon flux between the two model runs over time can be attributed to changes in surface ocean pCO_2 (green lines) from alterations to temperature (blue lines), DIC (red lines), alkalinity (yellow lines) and salinity (purple lines). These contributions are shown for the whole SO (C), the SO south of 40°S (D), and the SO north of 40°S (E).

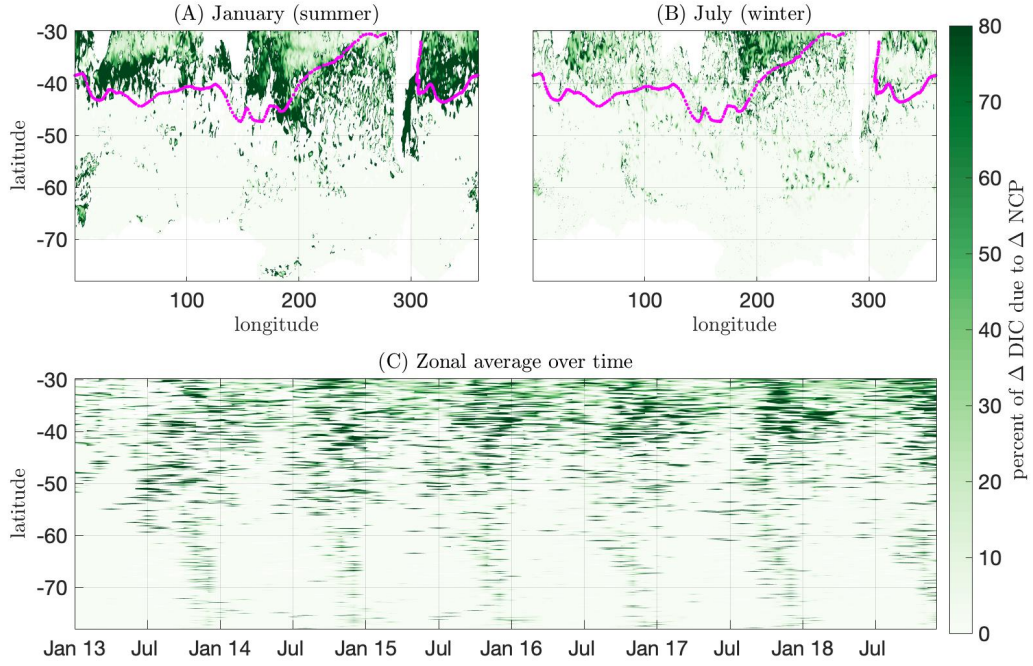


Figure 9: The percentage change of surface water DIC concentration due to changes in biological net community productivity (NCP). Surface water is defined here as waters down to a depth of 55m. Shown as a vertically integrated mean for (A) January (summer) and (B) July (winter). The mean location of the subtropical front, as defined by Orsi et al. (1995), is also shown in pink. (C) The zonal mean of the vertically integrated percentage change due to altered NCP is shown over time.

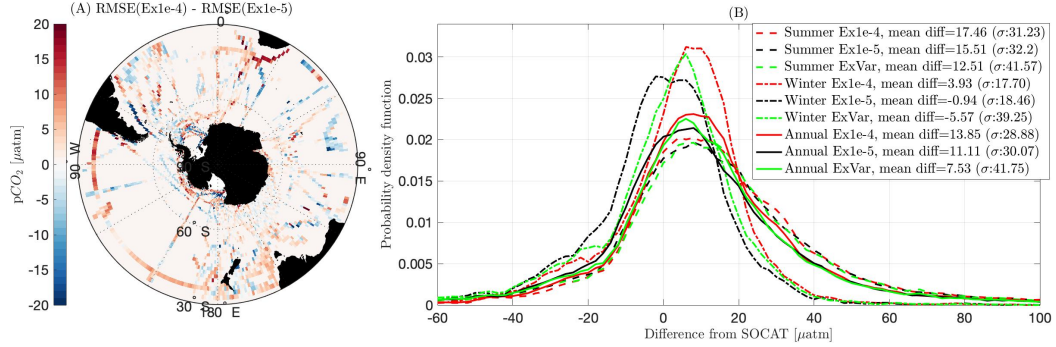


Figure 10: Comparison of modelled $p\text{CO}_2$ to observations from Surface Ocean CO_2 Atlas (SOCAT) between 2012 and 2018 (Bakker et al., 2016). (A) Comparison of the root mean squared error between Ex1e-4 and Ex1e-5. Red/blue shows regions where Ex1e-5/Ex1e-4 is closer to the observations. (B) Probability density function showing the misfit between observed carbon fluxes from SOCAT and the model outputs for $p\text{CO}_2$ in Ex1e-5 (black), Ex1e-4 (red), and ExVar (green).

1
2

3

4
5
6

7
8
9
10
11
12
13

Hypersensitivity of Southern Ocean air-sea carbon fluxes to background turbulent diapycnal mixing

Elizabeth Ellison¹, Ali Mashayek², Matthew Mazloff³

¹Imperial College London, Department of Civil and Environmental Engineering, London, UK
²University of Cambridge, Department of Earth Sciences, Cambridge, UK
³Scripps Institute of Oceanography, University of California San Diego, La Jolla, USA

Key Points:

- Total air-sea carbon fluxes in the Southern Ocean are altered by up to 66% annually by modest background mixing variations.
- Resolving or skillfully parameterising the spatiotemporal variability of small-scale turbulent mixing in the Southern Ocean is essential to model air-sea carbon fluxes.
- The spatiotemporal coverage of available $p\text{CO}_2$ observations is insufficient for constraining the role of diapycnal mixing rates below the mixed layer on air-sea fluxes

Abstract

The Southern Ocean (SO) connects major ocean basins and hosts large air-sea carbon fluxes due to the resurfacing of deep nutrient and carbon-rich waters. While surface-intensified wind-induced turbulent mixing in the SO surface mixed layer is significant for air-sea fluxes, the orders-of-magnitude weaker background mixing below the mixed layer has not been considered consequential. Topographically induced upward propagating lee waves in the SO, wind-induced downward propagating waves generated at the base of the mixed layer, shoaling of southward propagating internal tides generated in the basins north of the SO, and turbulence under sea ice are among the processes known to induce upper ocean background turbulence but typically are not represented in models. Here, we show that altering the background mixing in the SO over a modest range can lead to a $\sim 40\%$ - 60% annual change in SO air-sea CO_2 fluxes, with bigger changes on a seasonal timescale. This is primarily through altering the temperature and the dissolved inorganic carbon and alkalinity distribution in the surface water. Given the high spatiotemporal variability of processes that induce small-scale background mixing, this work demonstrates the importance of their representation in climate models for accurate simulation of global biogeochemical cycles.

Introduction

The Southern Ocean (SO), defined here as any region south of 30°S , is a key region for the global carbon cycle due to the upwelling of deep, old, carbon and nutrient-enriched waters, connecting the vast reservoir of nutrients and carbon from below the mixed layer with the surface (Talley et al., 2016). The deep ocean interacts with the atmosphere through less than 4% of the ocean's surface area (Watson & Naveira Garabato, 2006; Klocker, 2018), with 65% of interior waters making first contact with the atmosphere in the SO (DeVries & Primeau, 2011). As the deep ocean contains up to 60 times more carbon than the atmosphere (Arias et al., 2021), small perturbations to air-sea carbon fluxes can be important for atmospheric carbon content (Adkins, 2013). Therefore, the SO, and especially the upwelling branch of circumpolar deep water (Marshall & Speer, 2012), is key in controlling global biogeochemical cycles, the exchange of CO_2 between the atmosphere and the deep ocean, atmospheric CO_2 levels, and the response of the ocean and atmosphere to climate change (Sarmiento et al., 2004; Gruber et al., 2019).

Several expeditions have revealed strong cross-density (diapycnal) mixing due to small-scale ocean turbulence in the SO (Garabato et al., 2004; Ledwell et al., 2011; Watson et al., 2013; Garabato et al., 2019), though measurements remain sparse and difficult to scale up (Tamsitt et al., 2018; Mashayek et al., 2017; Cael & Mashayek, 2021; Mashayek et al., 2022). Given the small scales of diapycnal mixing, it is not resolved in operational models, and so it is parameterised (Gaspar, Grégoris, & Lefevre, 1990; W. G. Large et al., 1994) in two forms:

1. Surface mixed layer mixing from storms and other surface winds, as well as convective instabilities.
2. Background turbulence induced by bottom generated internal waves due to interaction of jets, eddies, and tides with rough topography or due to shoaling and breaking of remotely generated internal tides (see de Lavergne et al. (2020); Baker and Mashayek (2021, 2022) for reviews of such dynamics).

The ‘background’ mixing in the ocean interior is typically several orders of magnitude smaller than that in the surface mixed layers. Since the seminal work of Munk (1966), bulk measurements of ocean mixing have found a diapycnal turbulent diffusivity of $K_v \sim \mathcal{O}(10^{-4}) \text{ m}^2 \text{ s}^{-1}$ required to resurface the abyssal waters and facilitate the closure of the meridional overturning circulation (MOC) (Ganachaud & Wunsch, 2000; Talley et al., 2003; Lumpkin & Speer, 2007; Talley, 2013), while estimates from profiling instruments often find $K_v \sim \mathcal{O}(10^{-5}) \text{ m}^2 \text{ s}^{-1}$ in the interior of the ocean and much larger values only very close to

the seafloor (Waterhouse et al., 2014; Ferrari, 2014). In the Diapycnal and Isopycnal Mixing Experiment in the Southern Ocean (DIMES), estimates of mixing based on microstructure profiles reported $K_v \sim \mathcal{O}(10^{-5})m^2 s^{-1}$ at the mean depth of an anthropogenic tracer released upstream of the Drake Passage. Meanwhile, the tracer itself appeared to experience $K_v \sim \mathcal{O}(10^{-4})m^2 s^{-1}$ (Watson et al., 2013; Mashayek et al., 2017). The background values used in models typically lie within this range.

Though diapycnal mixing is highly temporally and spatially variable due to its generating mechanisms (e.g. strong surface westerly winds and interaction of the currents and eddies with rough topography), it is frequently parameterised as temporally invariable and, at times, even spatially constant. Current best estimates of SO diapycnal mixing are based on ‘static’ maps, produced with numerous limiting assumptions, approximating the contributions from topographically generated lee waves (Nikurashin & Ferrari, 2011; Shakespeare, 2020), wind-induced near-inertial waves (Alford, 2020), and internal tides (de Lavergne et al., 2020). These maps have formed the basis of our representation of such processes in earth system models (A. Melet et al., 2014; A. V. Melet et al., 2022).

Diapycnal mixing in the global ocean interior is known to be an important factor in variations in atmospheric carbon levels on centennial to millennial timescales via alterations in ocean circulation (Sigman et al., 2010; Marinov & Gnanadesikan, 2011). Enhanced diapycnal mixing increases deep ocean ventilation via the SO and reduces ocean carbon storage through biological and solubility carbon pumps (Marinov et al., 2008; Marinov & Gnanadesikan, 2011). Climate models are sensitive to the intensity and distribution of global diapycnal mixing, accounting for about 25% of the uncertainty in the estimated range of atmospheric CO_2 concentrations by 2100 (Schmittner et al., 2009). In this work, we are concerned with the response of the air-sea carbon fluxes to mixing below the surface mixed layer on time scales much shorter than those explored in the abovementioned works. We also solely focus on mixing in the SO which has been assumed to be of secondary importance for the global ocean circulation (Nikurashin & Ferrari, 2013) but significant for setting global tracer distributions (Ellison et al., 2021).

Given the strong wind-driven isopycnal upwelling in the Southern Ocean, and the intense diapycnal mixing within the mixed layer induced by strong winds, one may imagine that the modest background mixing below the mixed layer would be inconsequential for setting the air-sea fluxes of CO_2 on short timescales. In this work, we show the contrary. The air-sea flux of CO_2 primarily depends on the difference in the partial pressures of CO_2 (pCO_2) between the atmosphere and the ocean. Physical and biological processes, including advective and diffusive transport of tracers, organic matter formations and sinking, and the dilution of tracers due to precipitation, runoff and sea ice melt, all alter the pCO_2 of surface waters (Mahadevan et al., 2011), resulting in high variability in time and space of the CO_2 fluxes in the SO (Rosso et al., 2017). The influence of altering background diapycnal mixing on the surface ocean pCO_2 is complex to predict due to spatiotemporal variability in biological and physical responses to variations in mixing (Dutreuil et al., 2009), and the coupled multivariate dependency of ocean pCO_2 to temperature, salinity, alkalinity and dissolved inorganic carbon. In this work, we will show that modest perturbation of the background mixing strongly alters the SO-integrated air-sea CO_2 fluxes on seasonal, annual, and interannual timescales.

Experiment Setup

We use the Biogeochemical Southern Ocean state estimate (B-SOSE; Verdy and Mazloff (2017)). The interaction between diapycnal mixing below the mixed layer, the mixed layer dynamics, and the mesoscale processes that advect tracers prove essential for the problem under consideration here. Thus, employing an eddy-resolving model such as B-SOSE is essential and distinguishes this work from studies mentioned earlier that use low-resolution

models in global settings to study the role of mixing on carbon fluxes. In return, the timescales of relevance in our study are much shorter than theirs.

The model’s optimization procedure solves for adjustments to the prescribed atmospheric state and initial conditions to bring the solution into better consistency with observations. The resulting product is a closed-budget model simulation representing the present SO state. Because it represents the constantly evolving SO state it is not in a steady state, in contrast to what one may expect from analysis of an earth system model undergoing a long spin-up process. The B-SOSE simulation provides an estimate of SO biogeochemistry, including air-sea fluxes of heat and carbon and the cycling of nutrients from a biogeochemical and carbon model.

The model domain extends from the equator to 78°S with 52 vertical layers of varying thickness. The zonal grid spacing is always $1/6^\circ$, but the meridional grid spacing changes with the cosine of the latitude. Ocean physics is represented using the MITgcm. The ocean is forced through an atmospheric boundary layer scheme where bulk formulae determine heat fluxes, freshwater (salt), and momentum (W. Large & Yeager, 2009). The hourly atmospheric conditions of ERA5 (Dee et al., 2011) are applied, with adjustments added that were determined by optimization (Verdy & Mazloff, 2017) using the adjoint method. Sea ice is modelled using 0-layer thermodynamics (Fenty & Heimbach, 2013) and an implicit Line Successive Over Relaxation (LSOR) dynamical solver (Losch et al., 2010). A horizontal biharmonic diffusivity is used with a value of $10^{-8} \text{ m}^4\text{s}^{-1}$. Implicit vertical diffusivity for convection is set to $10 \text{ m}^2\text{s}^{-1}$, and no mesoscale eddy parameterisation was implemented. For further details, see Verdy and Mazloff (2017) and Swierczek et al. (2021).

The parameterisation of diapycnal mixing is composed of two parts. The GGL90 mixed layer parameterisation of Gaspar, Grégoris, and Lefevre (1990) is used to represent parameterised turbulence and is highly surface-enhanced (Fig.1 D), inducing strong turbulence under the seasonal atmospheric storm tracks, mixing the DIC gradients in the upper few hundreds of meters. In other places, such as under the ice or when there is no strong wind-induced turbulence, the models rely on a prescribed background value for turbulent diffusivity. The background value is behind the sensitivity of fluxes discussed in this work. As discussed in subsequent paragraphs, the background vertical diffusivity is altered in each experimental run. The background mixing value is added to the GGL90 mixing to achieve a total vertical diapycnal mixing value.

The Biogeochemistry with LIght, Nutrients and Gases (NBLING) model, described fully in Verdy and Mazloff (2017), forms the biochemical framework within B-SOSE. The original BLING model described in Galbraith et al. (2010) was modified (for B-SOSE) with the addition of nitrogen cycling and improvements in the representation of phytoplankton population dynamics and particle export (Galbraith et al., 2015; Bianchi et al., 2013). Biological activity influences the concentrations of carbon and oxygen. At the core of the BLING model is primary production with limitations by light, nitrate, phosphate, iron, and temperature, and subsequent remineralization of organic matter back to inorganic nutrients. Nine prognostic tracers are simulated in NBLING: dissolved inorganic carbon (DIC), alkalinity (ALK), oxygen (O_2), nitrate (NO_3), phosphate (PO_4), iron (Fe), dissolved organic nitrogen (DON), dissolved organic phosphate (DOP) and phytoplankton biomass. The biomass partitioning into species is determined using stored ratios updated every timestep based on growth and decay rates. We include three types of phytoplankton: large, small, and diazotrophs. Small cells represent calcifying organisms; they use calcium carbonate to form shells. Diazotrophs can fix nitrogen, so nitrate availability does not limit them. Phytoplankton loss is expressed as a power law with a size-dependent exponent based on (Dunne et al., 2005).

The B-SOSE carbon system is adapted from the MITgcm simple biogeochemical model of Dutkiewicz et al. (2006). DIC and ALK are prognostic variables, and pH and $p\text{CO}_2$ are diagnosed based on Follows et al. (2006), making oceanic $p\text{CO}_2$ a function of DIC,

ALK, temperature (T), salinity (S) and silica, where silica is prescribed from the 2013 World Ocean Atlas climatology (Garcia et al., 2013). CO₂ and oxygen air-sea fluxes are calculated following Wanninkhof (1992). Atmospheric $p\text{CO}_2$ is prescribed using values from the CarbonTracker product (Peters et al., 2007).

The state estimate is produced by solving for the model initial and boundary conditions, the so-called model ‘controls’, which minimize a weighted least squares sum of model-observation misfits. This is achieved using an adjoint model that provides the gradients of the misfit function with respect to the model controls, allowing those controls to be efficiently and systematically determined. The model is run for seven years (2012 - 2018) using the adjoint method-based assimilation product. This includes physical and biogeochemical constraints obtained from Argo floats, including biogeochemical parameters from the SOCCOM float array, satellite altimetry, satellite SST, and ship transect data. The full set of model parameters used in this 1/6° setup is given in Swierczek et al. (2021); see Verdy and Mazloff (2017) for initial conditions.

The B-SOSE’s original conditions and atmospheric adjustments were obtained using $10^{-4} \text{ m}^2 \text{ s}^{-1}$ as the value for background diapycnal diffusivity (added to the GGL90 mixing). We refer to that base simulation as Ex1e-4 hereafter. Using the same initial conditions and atmospheric state adjustments, two additional model simulations were carried out for 2013-2018. The first perturbation experiment, Ex1e-5, uses a constant background diffusivity value of $10^{-5} \text{ m}^2 \text{ s}^{-1}$. The range $10^{-5} \text{ m}^2 \text{ s}^{-1}$ to $10^{-4} \text{ m}^2 \text{ s}^{-1}$ is conservative, sandwiched between the two canonical paradigms of mixing often considered in Physical Oceanography. The third experiment, ExVar, uses a spatially variable (but temporally constant) vertical diapycnal mixing map (Fig 1A-C). The map is constructed as the sum of contributions from tides (de Lavergne et al., 2020) and topographically-generated lee waves (Nikurashin & Ferrari, 2013). ExVar features horizontal and vertical variations over a range much broader than $10^{-5} \text{ m}^2 \text{ s}^{-1}$ to $10^{-4} \text{ m}^2 \text{ s}^{-1}$. Although background mixing values dominate over the GGL90 parameterisation in mid-depths, GGL90 is orders of magnitude larger than the background mixing value in the upper ocean (Fig.1D). The three cases together allow for evaluating the impact of the magnitude of mixing and its spatial variations on the carbon flux independently.

Results

Carbon fluxes

The SO is a net sink of atmospheric CO₂, with most of the uptake occurring between 50°S and 30°S, with a peak at 40°S, where around 7 Tg C/yr is taken up (Fig.2A). 40°S is the average latitude of the subtropical front, separating the subtropical waters from the subantarctic mode waters, thus hosting rich mesoscale and submesoscale frontal dynamics and enhanced air-sea exchange of tracers. To the south of the polar front (panel E), on the other hand, the upwelling of deep carbon-rich waters causes carbon outgassing (shown in red panel E). Additional uptake occurs further south around Antarctica due to downwelling (induced by a change in the wind direction from westerly to easterly) and deep water formation. Thus, SO fronts, which mark sharp gradients in temperature and carbon chemistry, separate regions of net uptake from regions of outgassing. Higher latitudes show very low mean annual carbon fluxes, partly due to seasonal ice cover.

Carbon uptake varies year-on-year during the six years of the state estimate run by almost 2 Tg C/yr at some latitudes, with especially high inter-annual variability at 60°S and 40°S (Fig.2A). The inter-annual range of carbon fluxes for Ex1e-5 are highly non-monotonic. The inter-annual variations are due to varying oceanic conditions each year, some of which are associated with the Southern Annular Mode (SAM).

Alterations to background diapycnal mixing alter SO carbon fluxes, with ExVar showing smaller differences from Ex1e-5 than Ex1e-4 (Fig.2B dashed vs solid lines). The sensitivity

to altered diapycnal mixing is variable throughout the six years (Fig.2 B). This inter-annual range in sensitivity of around 0.1 Tg C/yr is well within the range of the inter-annual variability of zonally integrated carbon fluxes in Ex1e-5 (Fig.2A,B). A higher difference between Ex1e-5 and Ex1e-4, and to a lesser extent between Ex1e-5 and ExVar occurs in the first three years (2013 to 2015) than in the last three years (2016 to 2018) (Fig.2B). As upper ocean mixing is never in an equilibrium state due to constantly changing winds, eddies and buoyancy fluxes, the response to the mixing perturbation over the first few months of this experiment do not seem unrealistically exaggerated .

Increasing the background mixing from Ex1e-5 to Ex1e-4 leads to a reduction in annual mean zonally integrated carbon uptake at all latitudes (Fig.2C,F). The most significant reduction is around 55°S (Fig.2C,F). Minor changes occur south of 65°S due to the ice cover. In ExVar, the most significant changes from Ex1e-5 occur further north, at around 45°S. South of 60°S, the difference between ExVar and Ex1e-5 is insignificant (Fig.2C,G). Large areas of ExVar have carbon fluxes unchanged from those in Ex1e-5 (Fig.2G), suggesting that $10^{-4}m^2$ is likely too large of a background mixing value. In Ex1e-5, the mean annual cumulative net flux of carbon into the ocean, integrated from 75°S northward to 30°S, is 1 Pg C/yr (Fig.2D). In Ex1e-4 only 0.6 Pg C/yr is taken up, a reduction of 0.4 Pg C yr⁻¹. The annual uptake of ExVar falls between the other two experiments at around 0.8 Pg C/yr. These numbers are for the six-year mean, and as panel B shows, the reductions from Ex1e-5 are much higher over the first three years (almost double).

The cumulative carbon fluxes are compared to other estimates of the integrated SO carbon flux from 75°S northward to up to 45°S and 35°S for the period 2015-2017 (Fig.2D; Bushinsky et al. (2019); Landschützer et al. (2016); Rödenbeck et al. (2013)). At 45°S, the Ex1e-5 cumulative flux lies between the three observationally inferred estimates, while the ExVar flux is slightly lower, with Ex1e-4 being the lowest of all three, well below the estimates of the other studies. At 35°S, there is a larger range in carbon uptake between the three model runs. Ex1e-5 is the only experiment that lies within the bounds of the three observational estimates, though it appears towards the lower end, whilst ExVar and Ex1e-4 are below. This further suggests that the lower mixing in Ex1e-5 could be a more suitable background mixing value.

Changes to surface ocean pCO_2

Given that ExVar estimates of carbon fluxes fall between those of Ex1e-4 and Ex1e-5, hereafter, we only focus on the differences between Ex1e-4 and Ex1e-5. Air-sea carbon fluxes exist due to the difference in pCO_2 between the atmosphere and the surface ocean. The high (low) surface ocean pCO_2 values result in regions of low (high) oceanic uptake or even outgassing of CO_2 from the atmosphere (Fig.3A). A region of exception is under sea ice, where the diffusive flux of gases is prevented. The changes in carbon fluxes due to altered mixing, as in figure 2, are due to changes in surface ocean pCO_2 , as atmospheric conditions are constant across experiments.

The annual mean pCO_2 of the surface ocean is higher in Ex1e-4 than in Ex1e-5 in almost all regions, reducing the pCO_2 gradient and carbon uptake (Fig.3B). The areas of greatest increase in pCO_2 include south of South Africa and the waters east of the West Antarctic Peninsula. Small regions where the annual mean pCO_2 is reduced in Ex1e-4 include latitudes of around 30°S, especially to the east of Australia, the Argentine basin, and a few small bands just off the coast of Antarctica in the south.

Using the methodology set out by Takahashi et al. (2014), we break down the pCO_2 change to contributions from changes in the upper ocean content of salinity, temperature, DIC and alkalinity (equation 1). The change in pCO_2 as a contribution from each of the four tracers is calculated using equations 2-5, where $\bar{p}CO_2$ is the mean pCO_2 , \bar{Alk} is the mean alkalinity, γ_{CO_2} is the Revelle factor for CO_2 (value used = 11), and γ_{ALK} is the Revelle factor for alkalinity (value used = -10).

$$\begin{aligned}
\Delta pCO_2 &= \left(\frac{\delta pCO_2}{\delta T}\right)\Delta T + \left(\frac{\delta pCO_2}{\delta DIC}\right)\Delta DIC + \left(\frac{\delta pCO_2}{\delta Alk}\right)\Delta Alk + \left(\frac{\delta pCO_2}{\delta S}\right)\Delta S \quad (1) \\
\frac{\delta pCO_2}{\delta T}\Delta T &= 2(pCO_2)[Exp(0.0423(\pm 0.0002)\Delta T/2) - 1] \quad (2) \\
\left(\frac{\delta pCO_2}{\delta DIC}\right) &= \gamma_{CO_2}(\bar{p}CO_2/\bar{T}CO_2) \quad (3) \\
\frac{\delta pCO_2}{\delta Alk} &= \gamma_{ALK}(\frac{\bar{p}CO_2}{\bar{Alk}}) \quad (4) \\
\left(\frac{\delta pCO_2}{\delta S}\right) &= 0.026(\pm 0.002) \cdot \bar{p}CO_2 \quad (5)
\end{aligned}$$

The four individual contributions, shown in Fig.3D-G, can be summed together to give the annual mean approximated change in pCO_2 (Fig.3C). This calculated change agrees satisfactorily with the changes in pCO_2 between the two experiments (Fig.3B). This verifies the assumptions made in equations 2-5, and confirms that changes to the distribution of these tracers are key in causing changes to carbon fluxes (Fig.3B,C). The only region where the Takahashi et al. method does not capture the changes is in the north of the SO, west of New Zealand and east of South America in the Argentine basin. This is likely due to enhanced water mass mixing occurring in these regions, making changes in this area complex to approximate with simple assumptions. While the calculations shown in Fig. 3 use the upper 2.6 m of the water column, they are not sensitive to depth and similar results are found down to ~ 55 m.

On an annual basis, contributions from changes in DIC and alkalinity concentrations are the main drivers of changes in pCO_2 , with the contributions from salinity and temperature being secondary (Fig.3E,F). An increase in the alkalinity content decreases pCO_2 , whilst an increase in salinity or DIC increases pCO_2 . Where the temperature increases, pCO_2 increases due to modulation of the equilibrium DIC. The increase in the DIC content of the surface waters of the southern SO in Ex1e-4 increases pCO_2 , whilst in the north the decrease in DIC concentration decreases pCO_2 . On the contrary, the increase in alkalinity concentration in the south decreases pCO_2 , while the decrease in alkalinity in the north increases pCO_2 . Changes in salinity concentrations act to slightly increase the pCO_2 in Ex1e-4. Temperature changes with enhanced mixing cause a slight decrease in pCO_2 in the north and an increase in pCO_2 in the south in Ex1e-4.

Changes in the upper ocean temperature, salinity, DIC and alkalinity are due to alterations to the diapycnal flux of these tracers. The diapycnal flux for a tracer with concentration C may be approximated by $-K_v \times \frac{\partial C}{\partial z}$. Therefore, if vertical diapycnal mixing K_v is increased, more tracer, e.g. DIC, is mixed downgradient (upward into the surface waters). This increase in upward flux is the strongest where the vertical gradients are the strongest. Therefore, strong correlations develop between locations with sharp vertical gradients and locations with significantly altered tracer content with enhanced mixing (Fig.4A-D). This correlation is especially clear when examining changes to tracer distributions in the first month of the perturbation experiments, as shown in figure 4.

Regions that experience high changes in DIC concentration with enhanced mixing are around the coast of Antarctica, south of $60^\circ S$ and above depths of 40 m. In these areas, surface waters are fed by wind-induced upwelling of deep waters rich in DIC due to the respiration of organic material. Further to the north, the upper 120 m of the water column has weak vertical gradients of DIC concentration (Fig.4E,F). The dipole pattern shown when looking in a zonal average sense implies the erosion of the sharp gradient by enhanced mixing. The DIC concentration increases with increased mixing in the upper surface waters (shown in red), while concentrations decrease between 40m and 20m depth (shown in blue) due to a flux divergence, as more of this carbon has been mixed upwards into the surface waters (Fig.4G). There is a clear divide at around 20 m; this depth corresponds to the depth of the maximum vertical gradient. Changes in alkalinity and salinity roughly follow

a pattern similar to DIC (hence not shown). The greatest changes in temperature occur in different regions, mainly in the northern SO, especially at around 90°E, in the Argentine basin, and in the waters surrounding New Zealand.

Temporal and seasonal variability of changes in $p\text{CO}_2$

Carbon fluxes show strong seasonal and spatial variations (Fig.5), as for example, discussed in Rosso *et al.* (2017). In the austral summer (December to February), the SO from 60°S to 30°S is a net source of CO_2 outgassing (Fig.5A,B Dashed lines). Some outgassing also occurs at the upwelling zone of the polar front, especially in the Atlantic basin (Fig.5C). South of ~60°S, the SO acts as a slight carbon sink even in summer. Austral winter (June to August) has much higher carbon uptake than summer, with the net uptake occurring in almost all regions of the SO, except beneath sea ice (Fig.5A,B,D). Small outgassing regions exist around the polar front and at the upwelling region off the west coast of South America in the Argentine basin (Fig.5D).

While figures 2 and 3 show the changes to carbon fluxes between model runs in an annual mean sense, there are also significant temporal patterns in how mixing perturbation alters carbon fluxes (as will be discussed in Fig.8). Figures 5 and 6 examine the dominant mechanisms for seasonal differences observed in the changes to $p\text{CO}_2$ between Ex1e-4, ExVar and Ex1e-5. The changes in carbon fluxes between experiments are greater in winter than in summer (Fig.5A,E,F). An exception is in the very south, where ice cover during winter reduces gas exchange in all experiments. In winter, Ex1e-4 has a reduced carbon uptake compared to Ex1e-5, while ExVar has a similar carbon uptake to Ex1e-5 (Fig.5A). Cumulatively integrated winter carbon fluxes are reduced from almost 2 Pg C/yr in Ex1e-5 to 1.2 Pg C/yr in Ex1e-4. The greatest decreases in uptake occur around 40°S. The Argentine basin is also a region of pronounced diminished carbon uptake (Fig.5F). Three small areas on the edge of the winter ice extent experience increased carbon uptake in the winter due to reduced ice cover, the reason for which is explained subsequently (Blue areas, Fig.5F). Summer changes to carbon fluxes are of a smaller magnitude and show more spatial variability than the winter months (Fig.5A,E). In summer, the cumulative integrated outgassing of Ex1e-5 is higher than Ex1e-4, and ExVar is higher than both Ex1e-4 and Ex1e-5, though the difference between all three runs is less than 0.2 Pg C/yr. At lower latitudes where the SO is a net source of carbon to the atmosphere, outgassing is decreased in Ex1e-4. Further south, where the SO is a carbon sink, CO_2 uptake is reduced in Ex1e-4 (Fig.5E). Changes in flux occur as far south as the Antarctic continent due to diminished summer sea ice.

Using Eqs.1-5 and Fig. 3, we next use the Takahashi *et al.* methodology to examine seasonal changes to tracer contributions and their implications for the $p\text{CO}_2$ and carbon fluxes. The outcome is shown in Fig. 6. Salinity contributions to changes to $p\text{CO}_2$ are not shown as they are negligible compared to DIC, alkalinity, and temperature contributions. The temperature contribution varies greatly between seasons, being stronger in January than in July (Fig.6B,E). Closer to Antarctica, changes in temperature increase the $p\text{CO}_2$ of Ex1e-4 surface waters throughout the year. In July, this positive contribution extends further north. In January, the change in temperature causes very strong reductions in $p\text{CO}_2$, especially in the subtropical gyres. Because the change in surface temperature and associated change to $p\text{CO}_2$ vary with season, the annual mean change in temperature and its contribution to change in $p\text{CO}_2$ appear much smaller (Fig.3D). They are nevertheless key to driving the seasonal response of changing SO carbon fluxes in response to altered diapycnal mixing.

The vertical structure of the thermocline and the associated change in surface temperature with enhanced mixing have seasonal trends (Fig.7B,F). In January, surface waters are warm, and the temperature declines rapidly with depth down to 100 m, especially north of 60°S (Fig.7A). South of 60°S and below 100 m, water temperature increases with depth due to the upwelling of deep warm waters of North-Atlantic origin through Ekman transport.

In Ex1e-4, subsurface cooler waters are mixed more strongly towards the surface, cooling the surface waters and warming the subsurface waters relative to Ex1e-5 (Fig.7B). This surface cooling reduces the $p\text{CO}_2$ (Fig.6A). In July the surface waters are well mixed and there is no temperature gradient in the upper 100 m (Fig.7E). Below the winter mixed layer, temperature rises with depth. Enhanced mixing warms surface waters, increasing the $p\text{CO}_2$ (Fig.6E,F). This increase in surface temperature also increases the rate of sea ice melt, reducing the sea ice cover toward the end of winter/ spring in Ex1e-4. This results in small regions of increased carbon uptake around the sea ice edge in winter (Fig.5F). North of 60°S and below the mixed layer, waters still decrease in temperature with depth, so increased mixing cools the surface waters (Fig.7E,F). The vertical gradients of DIC and alkalinity are relatively constant regardless of season (Fig.7C,G). Changes in DIC and alkalinity concentrations have opposing effects on $p\text{CO}_2$ (Fig.3E,F), but together act to increase $p\text{CO}_2$ at all latitudes in summer and winter in Ex1e-4 (Fig.6C,F). The increase to $p\text{CO}_2$ in Ex1e-4 from combined carbonate chemistry changes is stronger in the winter than in summer, especially north of 40°S (Fig.6C,F).

Though all six years of the model run exhibit a similar seasonal cycle of changes to carbon fluxes with enhanced mixing in Ex1e-4, important inter-annual differences exist (Fig.8) which would not be appreciated in annual and seasonal means. Some differences in carbon fluxes between the two experiments become more pronounced over time, while other changes become less. North of 40°S , Ex1e-4 has an increase in carbon uptake (or reduced outgassing) during the summer. This becomes more pronounced and extends further south down to 50°S in subsequent summers as the model run progresses. While the winter time reductions in uptake in Ex1e-4 compared to Ex1e-5 around 45°S become stronger through the six years, the reductions in carbon uptake south of 60°S become weaker. The SO yearly mean change in C flux (red stars, Fig.8B) show a smaller mean change in the carbon flux between Ex1e-4 and Ex1e-5 in the later years of the run compared to earlier years. This is due to opposing signs of change to carbon fluxes over the seasons becoming more pronounced and therefore causing an antagonistic net effect to changes in an annual mean sense.

40°S approximately corresponds to the mean latitude of the subtropical front (STF) and marks a regime in terms of the leading mechanisms responsible for changes in $p\text{CO}_2$ and carbon fluxes. This marks the boundary between the nutrient deplete sub-tropical waters to the north and the nutrient and DIC rich waters to the south (Chapman et al., 2020). Regions to the north of this divide are responsible for the summer increases in carbon uptake in Ex1e-4 in later years of the run. In contrast, regions to the south are responsible for the strong response of reduced carbon uptake in Ex1e-4.

The contributions to the total change in $p\text{CO}_2$ are drastically different across the STF (Fig.8C-E). To its South, opposite changes in $p\text{CO}_2$ due to alkalinity and DIC nearly balance, with the latter being slightly larger (Fig.8D). As before, salinity contributions remain negligible at all times. Over the first two years of the perturbation, the total change in $p\text{CO}_2$ is positive, meaning $p\text{CO}_2$ is higher in Ex1e-4 than in Ex1e-5. The magnitude of the reduction in $p\text{CO}_2$ due to Alkalinity increases over time. The magnitude of total $p\text{CO}_2$ change decreases over time and becomes negative in the summer months, allowing for increased carbon uptake.

North of the STF, DIC and alkalinity do not balance each other out (Fig.8E) and changes in temperature between the two model runs are more dominant. Alkalinity increases $p\text{CO}_2$ north of the STF, while changes in DIC initially also increase the $p\text{CO}_2$ in Ex1e-4. By the summer of the third year of the run, changes in DIC begin to reduce the $p\text{CO}_2$, causing the net total change in $p\text{CO}_2$ to be negative in summer. This causes an increase in carbon uptake in the summer north of the STF in Ex1e-4.

Almost all changes in DIC between Ex1e-4 and Ex1e-5 are due to altered diapycnal fluxes of DIC. However, north of the STF, DIC contribution to decreased $p\text{CO}_2$ in the summer is due to increased productivity in the nutrient depleted waters of the sub tropical

gyre. This increase in productivity does not occur instantaneously, but instead takes around 6 months to begin decreasing the DIC contribution (red line, Fig.8E and Fig.9C). While an increase in productivity occurs with higher mixing across the whole SO region, it is only in the north, roughly north of the sub tropical front where increased phytoplankton production and DIC uptake becomes the dominant mechanism in altering DIC concentrations. Thus, in the context of this paper, we consider the STF as the upper boundary of the SO and postpone further discussion on the biologically-dominated change in $p\text{CO}_2$ north of the SO to future work.

Comparison to $p\text{CO}_2$ observational data

The $p\text{CO}_2$ values for Ex1e-4, Ex1e-5 and ExVar can be compared to 2013-2018 observed levels from the Surface Ocean CO_2 Atlas (SOCAT) (Bakker et al., 2016) (Fig.10). Neither clearly matches SOCAT observations better than the other (Fig.10A). Regional trends are also unclear, although from the limited data available, Ex1e-5 appears to better represent the $p\text{CO}_2$ of the northern Pacific Ocean, as well as off the coast of South Africa and Tasmania. Meanwhile estimates from Ex1e-4 are better matched to observations in the western Atlantic and the northern Indian Oceans.

The probability density function for the difference between SOCAT and B-SOSE for the three experiments is broken down over seasons (Fig.10B). In summer the standard deviation of differences between ExVar and data is much larger than those for Ex1e-4 and Ex1e-5. The mean difference of $15.5 \mu\text{atm}$ for Ex1e-5 is lower than $17.46 \mu\text{atm}$ for Ex1e-4, whilst ExVar has the lowest mean difference from observations. The high-end tails of the distributions are more skewed than the lower ends, implying a systematic over-estimate of $p\text{CO}_2$ by B-SOSE. B-SOSE overestimates the flux of carbon from the ocean to the atmosphere or underestimates the SO carbon uptake from the atmosphere, particularly in the summer.

SOCAT data is heavily biased towards summer data due to limitations on data collection in the winter. The mean difference between SOCAT and B-SOSE is lower for the winter mean than for the summer in all experiments. In the winter, ExVar has the largest mean difference from observations but also the largest standard deviation. In an annual mean sense, ExVar does a better job in matching SOCAT observations, though with a much higher standard deviation. It is interesting to note that, while in the annual mean sense, ExVar better matches SOCAT observations of $p\text{CO}_2$, Ex1e-5 was better able to replicate previous observational estimates of cumulative SO C fluxes (Fig.2D).

Conclusion

We have demonstrated that the air-sea carbon fluxes in the SO are highly sensitive to modest background mixing variations well within the range of our best estimates. This is despite background mixing rates being orders of magnitude smaller than mixed layer model generated mixing. We find that the overall changes to carbon fluxes depend on the interactive effects of changes to DIC, temperature, and alkalinity, which can compensate or reinforce each other, and the predominant driver varies regionally, seasonally and temporally as additive and opposing feedbacks kick in at varying time scales.

The relevance of diapycnal mixing in setting global carbon fluxes has previously been considered to be through changes to the underlying stratification and of regional and global overturning circulation and ventilation patterns. Although that may be true on centennial or longer timescales, here we show that on much faster timescales mixing directly acts upon tracers such as DIC, alkalinity, temperature, and salinity leading to a significant change in surface ocean carbon fluxes.

The high correlation found between vertical gradients and strong changes in tracer distributions with altered mixing shows that on a timescale of days to months, direct changes

in diapycnal mixing fluxes are the predominant drivers of the $p\text{CO}_2$ response in the SO. On longer timescales, from months to years, further feedbacks involving changes to biological productivity and mixed layer depth will also begin to cause further changes to the surface ocean $p\text{CO}_2$. A latitudinal divide exists at around 40°S , roughly the location of the subtropical front. High vertical tracer gradients cause the direct impact of altered tracer fluxes to dominate trends to the south, whilst changes in biological productivity play a key role in the observed changes to carbon fluxes to the north.

Two major issues stand in the way of better constraining of the data-assimilating ocean estimates insofar as the role of vertical mixing in the upper ocean is concerned. First, despite the significant investments in observations such as SOCAT, Fig. 10A clearly shows the sparsity of the available observational data. From a statistical perspective, this coverage is insufficient to discern which background mixing value better represents the real ocean despite the strong impact of these choices on $p\text{CO}_2$. This issue can be resolved only through sustained observations. Knowledge of the seasonal cycle of $p\text{CO}_2$ is worse in the SO than in most other regions of the ocean. The strong seasonality of the sensitivity of carbon fluxes to altered mixing demonstrates the importance of year-round observations. Second, SO diapycnal mixing can vary by orders of magnitude over timescales ranging from hourly to seasonally, as well as varying spatially. To achieve a close agreement with observations, a model should have a representation of such variability. ExVar employed our best estimate of a time-mean spatially variable mixing map, resulting in carbon fluxes similar to that obtained with a constant diffusivity of $10^{-5}\text{m}^2/\text{s}$. Direct observations of diapycnal mixing in the SO have suggested that such maps (a) lack the representation of many key processes that result in higher turbulence in upper surface waters (e.g. bottom-generated lee waves, shoaling of remotely generated internal tides) and (b) do not allow for co-variance of mixing and tracer gradients, key to biological processes. This work highlights the absolute necessity for climate models to resolve the spatio-temporal variability of small-scale turbulent mixing, or to skillfully parameterise the processes responsible for generating them.

1 Data and material availability

The data sets generated during and/or analysed during the current study are available from the corresponding author on reasonable request and from <http://sose.ucsd.edu>.

The data used to construct the spatially variable mixing map used for ExVar is available at <https://agupubs.onlinelibrary.wiley.com/doi/full/10.1029/2020MS002065>.

References

- Adkins, J. F. (2013, 9). The role of deep ocean circulation in setting glacial climates. *Paleoceanography*, 28(3), 539–561. Retrieved from <http://doi.wiley.com/10.1002/palo.20046> doi: 10.1002/palo.20046
- Alford, M. H. (2020). Global calculations of local and remote near-inertial-wave dissipation. *Journal of Physical Oceanography*, 50(11), 3157–3164.
- Arias, P., Bellouin, N., Coppola, E., Jones, R., Krinner, G., Marotzke, J., ... others (2021). Climate change 2021: The physical science basis. contribution of working group 14 i to the sixth assessment report of the intergovernmental panel on climate change; technical summary.
- Baker, L., & Mashayek, A. (2021). Surface reflection of bottom generated oceanic lee waves. *Journal of Fluid Mechanics*, 924, A17.
- Baker, L., & Mashayek, A. (2022). The impact of realistic topographic representation on the parameterisation of oceanic lee wave energy flux. *Authorea Preprints*.
- Bakker, D. C., Pfeil, B., Landa, C. S., Metzl, N., O'Brien, K. M., Olsen, A., ... Xu, S. (2016, sep). *A multi-decade record of high-quality $f\text{CO}_2$ data in version 3 of the Surface Ocean CO_2 Atlas (SOCAT)* (Vol. 8) (No. 2). Retrieved from <https://essd.copernicus.org/articles/8/383/2016/> doi: 10.5194/essd-8-383-2016

- Bianchi, D., Galbraith, E. D., Carozza, D. A., Mislan, K., & Stock, C. A. (2013). Intensification of open-ocean oxygen depletion by vertically migrating animals. *Nature Geoscience*, 6(7), 545–548.
- Bushinsky, S. M., Landschützer, P., Rödenbeck, C., Gray, A. R., Baker, D., Mazloff, M. R., ... Sarmiento, J. L. (2019, 11). Reassessing Southern Ocean Air-Sea CO₂ Flux Estimates With the Addition of Biogeochemical Float Observations. *Global Biogeochemical Cycles*, 33(11), 1370–1388. Retrieved from <https://onlinelibrary.wiley.com/doi/abs/10.1029/2019GB006176> doi: 10.1029/2019GB006176
- Cael, B., & Mashayek, A. (2021). Log-skew-normality of ocean turbulence. *Physical Review Letters*, 126(22), 224502.
- Chapman, C. C., Lea, M. A., Meyer, A., Sallée, J. B., & Hindell, M. (2020). Defining Southern Ocean fronts and their influence on biological and physical processes in a changing climate. *Nature Climate Change*. doi: 10.1038/s41558-020-0705-4
- Dee, D. P., Uppala, S. M., Simmons, A. J., Berrisford, P., Poli, P., Kobayashi, S., ... others (2011). The era-interim reanalysis: Configuration and performance of the data assimilation system. *Quarterly Journal of the royal meteorological society*, 137(656), 553–597.
- de Lavergne, C., Vic, C., Madec, G., Roquet, F., Waterhouse, A. F., Whalen, C. B., ... Hibiya, T. (2020, 5). A Parameterization of Local and Remote Tidal Mixing. *Journal of Advances in Modeling Earth Systems*, 12(5), e2020MS002065. Retrieved from <https://onlinelibrary.wiley.com/doi/abs/10.1029/2020MS002065> doi: 10.1029/2020MS002065
- DeVries, T., & Primeau, F. (2011, 12). Dynamically and Observationally Constrained Estimates of Water-Mass Distributions and Ages in the Global Ocean. *Journal of Physical Oceanography*, 41(12), 2381–2401. Retrieved from <https://journals.ametsoc.org/jpo/article/41/12/2381/11258/Dynamically-and-Observationally-Constrained> doi: 10.1175/JPO-D-10-05011.1
- Dunne, J. P., Armstrong, R. A., Gnanadesikan, A., & Sarmiento, J. L. (2005). Empirical and mechanistic models for the particle export ratio. *Global Biogeochemical Cycles*, 19(4).
- Dutkiewicz, S., Follows, M. J., Heimbach, P., & Marshall, J. (2006). Controls on ocean productivity and air-sea carbon flux: An adjoint model sensitivity study. *Geophysical Research Letters*, 33(2).
- Dutreuil, S., Bopp, L., & Tagliabue, A. (2009). Impact of enhanced vertical mixing on marine biogeochemistry: Lessons for geo-engineering and natural variability. *Biogeosciences*, 6(5), 901–912. Retrieved from www.biogeosciences.net/6/901/2009/ doi: 10.5194/bg-6-901-2009
- Ellison, E., Mashayekh, A., & Cimolo, L. (2021). Multi-timescale control of southern ocean diapycnal mixing over atlantic tracer budgets.
- Fenty, I., & Heimbach, P. (2013). Coupled sea ice–ocean-state estimation in the labrador sea and baffin bay. *Journal of physical oceanography*, 43(5), 884–904.
- Ferrari, R. (2014). *Oceanography: What goes down must come up*. doi: 10.1038/513179a
- Follows, M. J., Ito, T., & Dutkiewicz, S. (2006, jan). On the solution of the carbonate chemistry system in ocean biogeochemistry models. *Ocean Modelling*, 12(3-4), 290–301. Retrieved from <https://www.sciencedirect.com/science/article/abs/pii/S1463500305000533> doi: 10.1016/J.OCEMOD.2005.05.004
- Galbraith, E. D., Dunne, J. P., Gnanadesikan, A., Slater, R. D., Sarmiento, J. L., Dufour, C. O., ... others (2015). Complex functionality with minimal computation: Promise and pitfalls of reduced-tracer ocean biogeochemistry models. *Journal of Advances in Modeling Earth Systems*, 7(4), 2012–2028.
- Galbraith, E. D., Gnanadesikan, A., Dunne, J. P., & Hiscock, M. R. (2010). Regional impacts of iron-light colimitation in a global biogeochemical model. *Biogeosciences*, 7(3), 1043–1064.
- Ganachaud, A., & Wunsch, C. (2000). Improved estimates of global ocean circulation, heat

- transport and mixing from hydrographic data. *Nature*, 408(6811), 453–457.
- Garabato, A. C. N., Frajka-Williams, E. E., Spingys, C. P., Legg, S., Polzin, K. L., Forryan, A., ... others (2019). Rapid mixing and exchange of deep-ocean waters in an abyssal boundary current. *Proceedings of the National Academy of Sciences*, 116(27), 13233–13238.
- Garabato, A. C. N., Polzin, K. L., King, B. A., Heywood, K. J., & Visbeck, M. (2004). Widespread intense turbulent mixing in the southern ocean. *Science*, 303(5655), 210–213.
- Garcia, H. E., Locarnini, R. A., Boyer, T. P., Antonov, J. I., Baranova, O. K., Zweng, M. M., ... Levitus, S. (2013). World ocean atlas 2013. volume 4, dissolved inorganic nutrients (phosphate, nitrate, silicate).
- Gaspar, P., Grégoris, Y., & Lefevre, J.-M. (1990). A simple eddy kinetic energy model for simulations of the oceanic vertical mixing: Tests at station papa and long-term upper ocean study site. *Journal of Geophysical Research: Oceans*, 95(C9), 16179–16193.
- Gaspar, P., Grégoris, Y., & Lefevre, J.-M. (1990, sep). A simple eddy kinetic energy model for simulations of the oceanic vertical mixing: Tests at station Papa and long-term upper ocean study site. *Journal of Geophysical Research*, 95(C9), 16179. Retrieved from <http://doi.wiley.com/10.1029/JC095iC09p16179> doi: 10.1029/JC095iC09p16179
- Gruber, N., Landschützer, P., & Lovenduski, N. S. (2019). The variable southern ocean carbon sink. *Annual review of marine science*, 11, 159–186.
- Klocker, A. (2018). Opening the window to the Southern Ocean: The role of jet dynamics. *Science Advances*. doi: 10.1126/sciadv.aao4719
- Landschützer, P., Gruber, N., & Bakker, D. C. E. (2016, 10). Decadal variations and trends of the global ocean carbon sink. *Global Biogeochemical Cycles*, 30(10), 1396–1417. Retrieved from <http://doi.wiley.com/10.1002/2015GB005359> doi: 10.1002/2015GB005359
- Large, W., & Yeager, S. (2009). The global climatology of an interannually varying air–sea flux data set. *Climate dynamics*, 33(2), 341–364.
- Large, W. G., McWilliams, J. C., & Doney, S. C. (1994). Oceanic vertical mixing: A review and a model with a nonlocal boundary layer parameterization. *Reviews of geophysics*, 32(4), 363–403.
- Ledwell, J. R., St. Laurent, L. C., Garton, J. B., & Toole, J. M. (2011). Diapycnal mixing in the antarctic circumpolar current. *Journal of Physical Oceanography*, 41(1), 241–246. Retrieved from <http://www.rocklandscientific.com> doi: 10.1175/2010JPO4557.1
- Losch, M., Menemenlis, D., Campin, J.-M., Heimbach, P., & Hill, C. (2010). On the formulation of sea-ice models. part 1: Effects of different solver implementations and parameterizations. *Ocean Modelling*, 33(1-2), 129–144.
- Lumpkin, R., & Speer, K. (2007). Global ocean meridional overturning. *Journal of Physical Oceanography*, 37(10), 2550–2562.
- Mahadevan, A., Tagliabue, A., Bopp, L., Lenton, A., Mémer, L., & Lévy, M. (2011, 5). Impact of episodic vertical fluxes on sea surface pCO₂. *Philosophical Transactions of the Royal Society A: Mathematical, Physical and Engineering Sciences*, 369(1943), 2009–2025. Retrieved from <https://royalsocietypublishing.org/doi/10.1098/rsta.2010.0340> doi: 10.1098/rsta.2010.0340
- Marinov, I., & Gnanadesikan, A. (2011, 2). Changes in ocean circulation and carbon storage are decoupled from air–sea CO₂ fluxes. *Biogeosciences*, 8(2), 505–513. Retrieved from <https://bg.copernicus.org/articles/8/505/2011/> doi: 10.5194/bg-8-505-2011
- Marinov, I., Gnanadesikan, A., Sarmiento, J. L., Toggweiler, J. R., Follows, M., & Mignone, B. K. (2008). Impact of oceanic circulation on biological carbon storage in the ocean and atmospheric pCO₂. *Global Biogeochemical Cycles*. doi: 10.1029/2007GB002958
- Marshall, J., & Speer, K. (2012). Closure of the meridional overturning circulation through Southern Ocean upwelling. *Nature Geoscience*, 5(3), 171–180. Retrieved from [www](http://www.nature.com)

- .nature.com/naturegeoscience doi: 10.1038/ngeo1391
- Mashayek, A., Ferrari, R., Merrifield, S., Ledwell, J., St Laurent, L., & Garabato, A. (2017). Topographic enhancement of vertical turbulent mixing in the Southern Ocean. *Nature Communications*, 8. doi: 10.1038/ncomms14197
- Mashayek, A., Reynard, N., Zhai, F., Srinivasan, K., Jelley, A., Garabato, A. N., & Caulfield, C.-c. P. (2022). Deep ocean learning of small scale turbulence. *Geophysical Research Letters*, e2022GL098039.
- Melet, A., Hallberg, R., Legg, S., Nikurashin, M., Melet, A., Hallberg, R., ... Nikurashin, M. (2014, 3). Sensitivity of the Ocean State to Lee Wave–Driven Mixing. *Journal of Physical Oceanography*, 44(3), 900–921. Retrieved from <http://journals.ametsoc.org/doi/abs/10.1175/JPO-D-13-072.1> doi: 10.1175/JPO-D-13-072.1
- Melet, A. V., Hallberg, R., & Marshall, D. P. (2022). The role of ocean mixing in the climate system. In *Ocean mixing* (pp. 5–34). Elsevier.
- Munk, W. H. (1966). Abyssal recipes. In *Deep sea research and oceanographic abstracts* (Vol. 13, pp. 707–730).
- Nikurashin, M., & Ferrari, R. (2011). Global energy conversion rate from geostrophic flows into internal lee waves in the deep ocean. *Geophysical Research Letters*, 38(8).
- Nikurashin, M., & Ferrari, R. (2013). Overturning circulation driven by breaking internal waves in the deep ocean. *Geophysical Research Letters*, 40(12), 3133–3137.
- Orsi, A. H., Whitworth, T., & Nowlin, W. D. (1995, may). On the meridional extent and fronts of the Antarctic Circumpolar Current. *Deep Sea Research Part I: Oceanographic Research Papers*, 42(5), 641–673. Retrieved from <https://www.sciencedirect.com/science/article/pii/096706379500021W> doi: 10.1016/0967-0637(95)00021-W
- Peters, W., Jacobson, A. R., Sweeney, C., Andrews, A. E., Conway, T. J., Masarie, K., ... others (2007). An atmospheric perspective on north american carbon dioxide exchange: Carbontracker. *Proceedings of the National Academy of Sciences*, 104(48), 18925–18930.
- Rödenbeck, C., Keeling, R. F., Bakker, D. C., Metzl, N., Olsen, A., Sabine, C., & Heimann, M. (2013). Global surface-ocean p co₂ and sea–air co₂ flux variability from an observation-driven ocean mixed-layer scheme. *Ocean Science*, 9(2), 193–216.
- Rosso, I., Mazloff, M. R., Verdy, A., & Talley, L. D. (2017, sep). Space and time variability of the Southern Ocean carbon budget. *Journal of Geophysical Research: Oceans*, 122(9), 7407–7432. Retrieved from <http://doi.wiley.com/10.1002/2016JC012646> doi: 10.1002/2016JC012646
- Sarmiento, J. L., Gruber, N., Brzezinski, M. A., & Dunne, J. P. (2004). High-latitude controls of thermocline nutrients and low latitude biological productivity. *Nature*. doi: 10.1038/nature02127
- Schmittner, A., Urban, N. M., Keller, K., & Matthews, D. (2009). Using tracer observations to reduce the uncertainty of ocean diapycnal mixing and climate-carbon cycle projections. *Global Biogeochemical Cycles*, 23(4). Retrieved from <http://www.nodc.org> doi: 10.1029/2008GB003421
- Shakespeare, C. J. (2020). Interdependence of internal tide and lee wave generation at abyssal hills: Global calculations. *Journal of Physical Oceanography*, 50(3), 655–677.
- Sigman, D. M., Hain, M. P., & Haug, G. H. (2010). *The polar ocean and glacial cycles in atmospheric CO₂ concentration* (Vol. 466) (No. 7302). doi: 10.1038/nature09149
- Swierczek, S., Mazloff, M. R., Morzfeld, M., & Russell, J. L. (2021, jul). The effect of resolution on vertical heat and carbon transports in a regional ocean circulation model of the argentine basin. *Journal of Geophysical Research: Oceans*, 126(7), e2021JC017235. Retrieved from <https://onlinelibrary.wiley.com/doi/10.1029/2021JC017235> doi: 10.1029/2021jc017235
- Takahashi, T., Sutherland, S. C., Chipman, D. W., Goddard, J. G., & Ho, C. (2014). Climatological distributions of pH, pCO₂, total CO₂, alkalinity, and CaCO₃ saturation in the global surface ocean, and temporal changes at selected locations. *Marine Chemistry*. doi: 10.1016/j.marchem.2014.06.004
- Talley, L. D. (2013). Closure of the global overturning circulation through the Indian,

- 675 Pacific, and southern oceans. *Oceanography*, 26(1), 80–97. Retrieved from [http://](http://dx.doi.org/10.5670/oceanog.2013.07)
676 dx.doi.org/10.5670/oceanog.2013.07 doi: 10.5670/oceanog.2013.07
- 677 Talley, L. D., Feely, R. A., Sloyan, B. M., Wanninkhof, R., Baringer, M. O., Bullister,
678 J. L., ... Zhang, J. Z. (2016, 1). Changes in Ocean Heat, Carbon Content, and
679 Ventilation: A Review of the First Decade of GO-SHIP Global Repeat Hydrography.
680 *Annual Review of Marine Science*, 8, 185–215. Retrieved from www.go-ship.org doi:
681 10.1146/annurev-marine-052915-100829
- 682 Talley, L. D., Reid, J. L., & Robbins, P. E. (2003). Data-based meridional overturning
683 streamfunctions for the global ocean. *Journal of Climate*, 16(19), 3213–3226.
- 684 Tamsitt, V., Abernathey, R. P., Mazloff, M. R., Wang, J., & Talley, L. D. (2018). Transfor-
685 mation of Deep Water Masses Along Lagrangian Upwelling Pathways in the Southern
686 Ocean. *Journal of Geophysical Research: Oceans*. doi: 10.1002/2017JC013409
- 687 Verdy, A., & Mazloff, M. R. (2017). A data assimilating model for estimating Southern
688 Ocean biogeochemistry. *Journal of Geophysical Research: Oceans*, 122(9), 6968–6988.
689 Retrieved from <http://hycom.org> doi: 10.1002/2016JC012650
- 690 Wanninkhof, R. (1992). Relationship between wind speed and gas exchange over the ocean.
691 *Journal of Geophysical Research: Oceans*, 97(C5), 7373–7382.
- 692 Waterhouse, A. F., Mackinnon, J. A., Nash, J. D., Alford, M. H., Kunze, E., Simmons,
693 H. L., ... Lee, C. M. (2014). Global patterns of diapycnal mixing from measurements
694 of the turbulent dissipation rate. *Journal of Physical Oceanography*. doi: 10.1175/
695 JPO-D-13-0104.1
- 696 Watson, A. J., Ledwell, J. R., Messias, M. J., King, B. A., Mackay, N., Meredith, M. P., ...
697 Garabato, A. C. N. (2013). Rapid cross-density ocean mixing at mid-depths in the
698 Drake Passage measured by tracer release. *Nature*, 501(7467), 408–411.
- 699 Watson, A. J., & Naveira Garabato, A. C. (2006). The role of Southern Ocean mixing and
700 upwelling in glacial-interglacial atmospheric CO₂ change. *Tellus, Series B: Chemical*
701 *and Physical Meteorology*, 58(1), 73–87. Retrieved from [https://www.tandfonline](https://www.tandfonline.com/action/journalInformation?journalCode=zclb20)
702 [.com/action/journalInformation?journalCode=zclb20](https://www.tandfonline.com/action/journalInformation?journalCode=zclb20) doi: 10.1111/j.1600-0889
703 .2005.00167.x

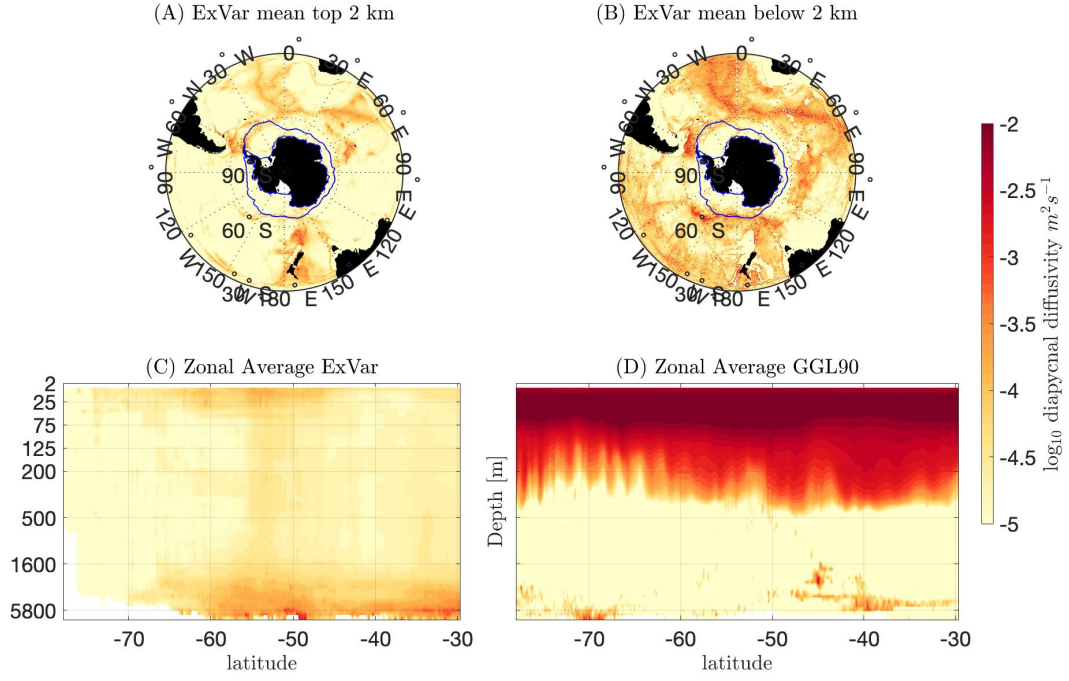


Figure 1: Diapycnal mixing in the Southern Ocean State Estimate (SOSE). The distribution of diapycnal mixing in the Southern ocean, constructed as the sum of contributions from tides and topographically-generated lee waves. This mixing is shown averaged in depth over the top/bottom 2km in panel *A/B*, and zonally over the Southern Ocean in *C*. These maps are used in the spatially variable mixing map experiment (ExVar). For reference, a zonally-averaged map of the storm-induced mixing, as parameterised through GGL90 parameterisation in B-SOSE, is also shown in panel *D*.

704

705

706

707

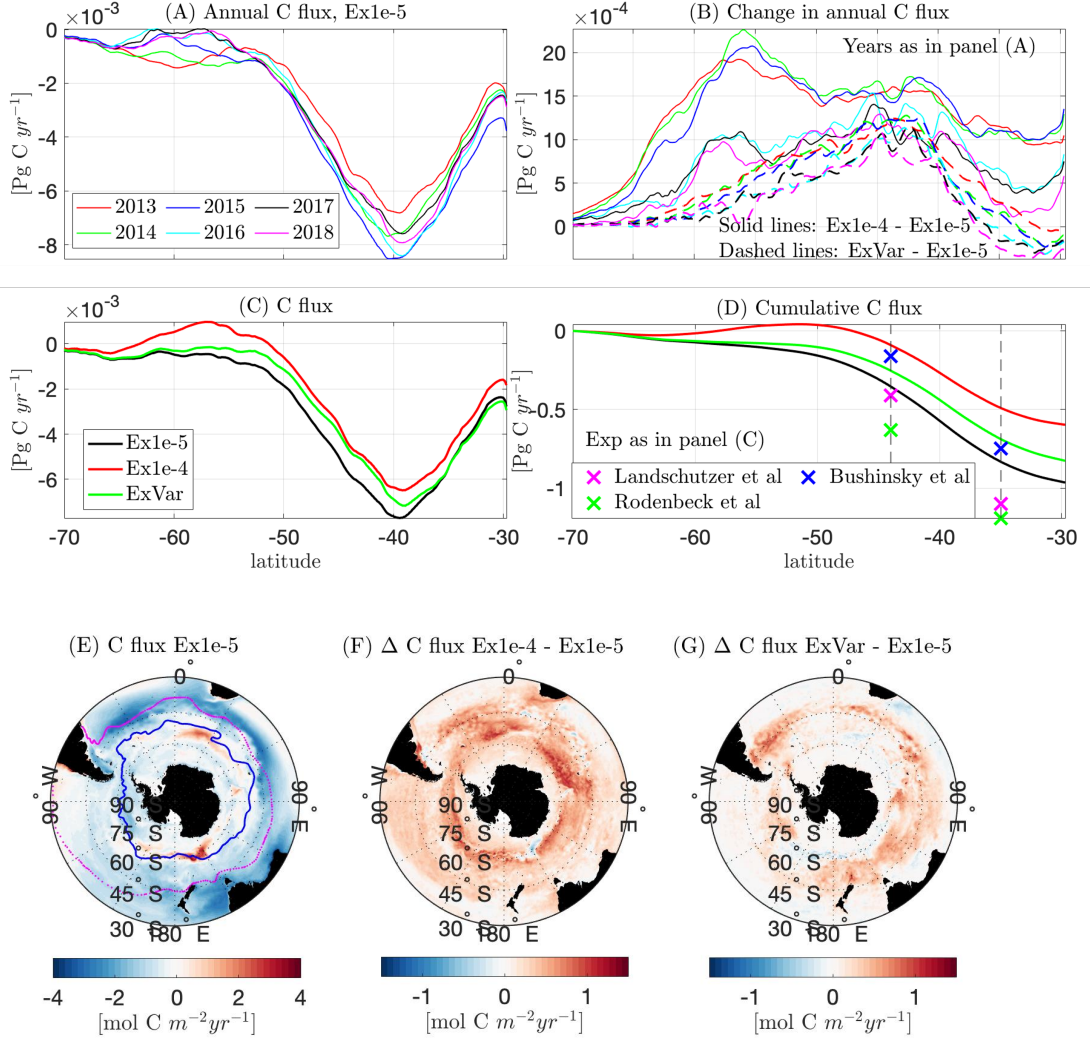


Figure 2: (A) Zonally integrated flux of Carbon for each year of Ex1e-5 (negative = Carbon flux from atmosphere to ocean). (B) Difference in the zonally integrated flux of Carbon between Ex1e-4 and Ex1e-5 (solid lines) and ExVar and Ex1e-5 (dashed lines) for each year of the experiment. (C) zonally integrated annual mean (2013-2018) Carbon flux for Ex1e-4, Ex1e-5 and ExVar. (D) Annual mean (averaged over 2013 to 2018) cumulative integral of carbon fluxes from 70°S northward to 30°S (legend same as the previous panel). Observational markers are included for comparison (Landschützer et al., 2016; Bushinsky et al., 2019; Rödenbeck et al., 2013). (E) Average annual carbon flux for Ex1e-5, the blue line shows the Polar Front, the magenta line shows Sub-tropical Front as defined by Orsi et al. (1995). (F) Annual mean change in Carbon flux (Ex1e-4 – Ex1e-5). (G) Annual mean change in Carbon flux (ExVar – Ex1e-5). Positive values imply reduced carbon uptake or increased outgassing.

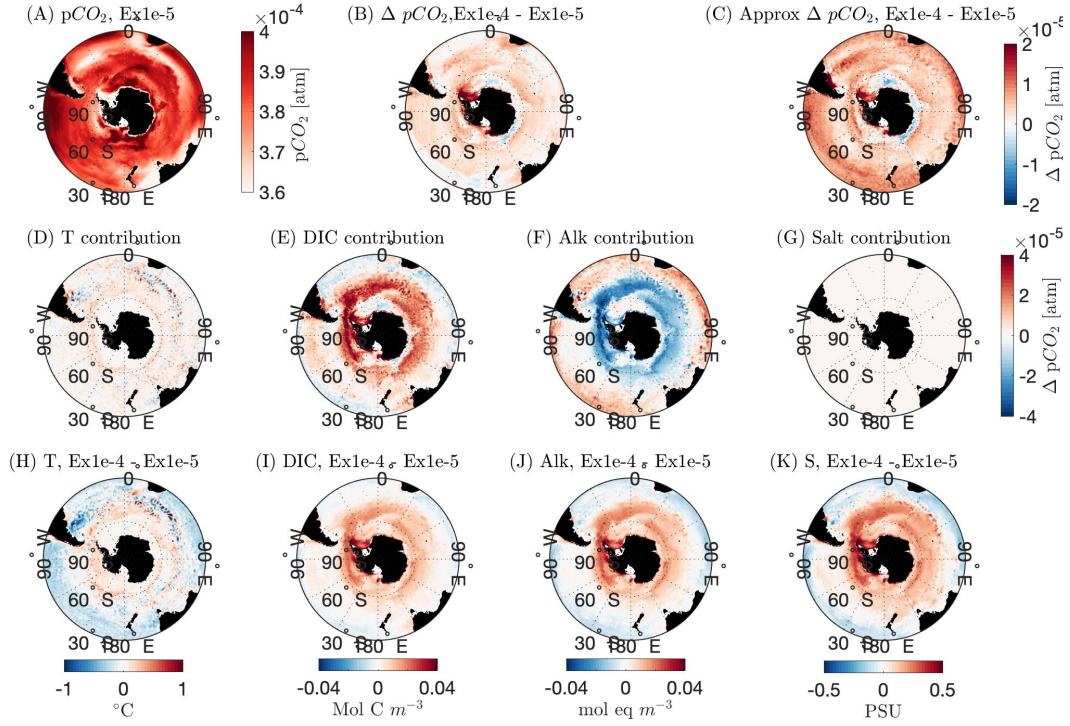


Figure 3: Changes to surface ocean partial pressure and carbon fluxes. (A) Annual mean surface ocean $p\text{CO}_2$ in Ex1e-5. (B) Change in $p\text{CO}_2$ between Ex1e-4 and Ex1e-5. (C) Same as panel B, but this time changes to $p\text{CO}_2$ approximated based on the methodology of Takahashi et al. (2014) that breaks down the change into various contributions as per equations (1-5). The various contributions are shown in panels D-G. (H-K) Changes in annual mean DIC, alkalinity, potential temperature and salinity.

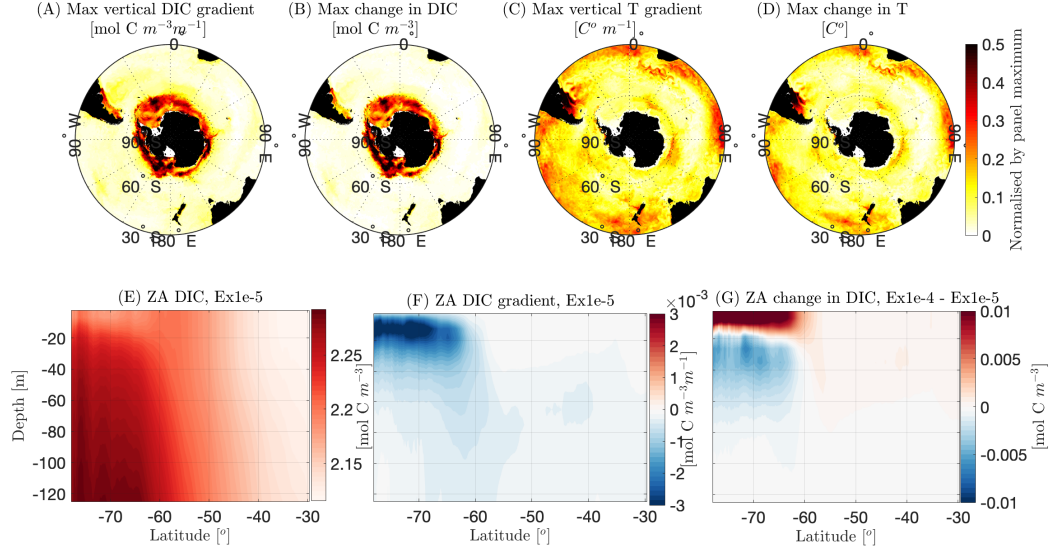


Figure 4: (A) Maximum vertical DIC gradient in the water column for Ex1e-5, normalised by maximum contour value. (B) Maximum change in DIC between Ex1e-4 and Ex1e-5, normalised by the maximum contour value. (C,D) Same as A and B but for temperature. The maximum change in DIC (temperature) is defined as the greatest difference in DIC (temperature) concentration between the two experiments at any depth above 200 m at each latitude and longitude in the domain. (E) Zonal average DIC concentration in Ex1e-5. (F) Zonal average DIC vertical gradient in Ex1e-5; blue indicates a decrease in concentration towards the surface. (G) Zonally averaged change in DIC concentration (Ex1e-4 - Ex1e-5). All shown for December 2012, the first month of all experiments.

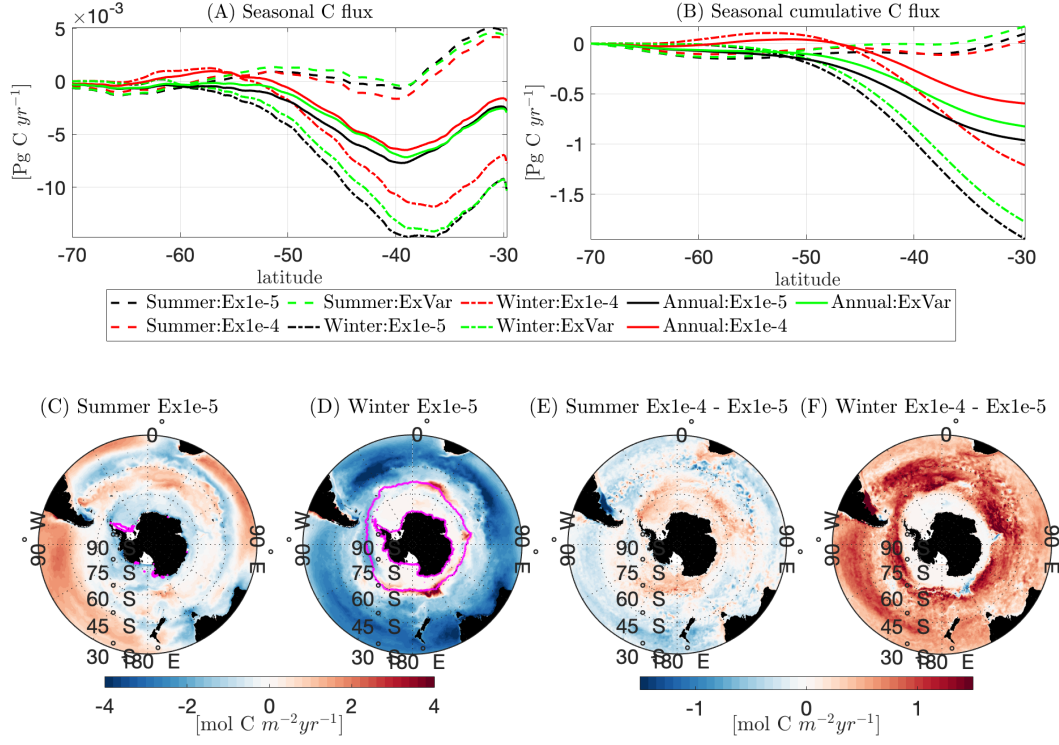


Figure 5: (A) zonally integrated Carbon flux for Ex1e-4, Ex1e-5 and ExVar for summer (dashed), winter (Dotted), and annual mean (solid line). (B) Cumulative sum of carbon fluxes from 70°S northward to 30°S (legend same as the previous panel). (C) Average summer carbon flux for Ex1e-5; magenta lines show the minimum summer ice extent. (D) Average winter carbon flux for Ex1e-5; magenta lines show the maximum winter ice extent. (E) Mean change in summer Carbon flux (Ex1e-4 - Ex1e-5). (F) Mean change in winter Carbon flux (Ex1e-4 - Ex1e-5). Positive values imply reduced carbon uptake or increased outgassing.

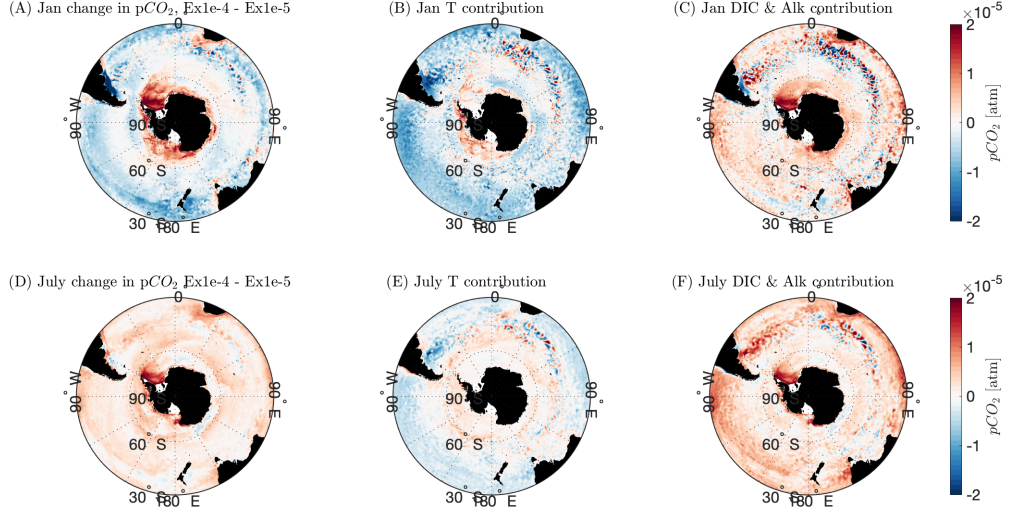


Figure 6: (A) January (summer) 2013-2018 mean change in $p\text{CO}_2$ (Ex1e-4 - Ex1e-5) approximated by the method of Takahashi et al. (2014). (B) Contribution due to changes in temperature. (C) Contribution due to changes in carbon chemistry (DIC and Alkalinity). (D-F) Same as A-C but for July (winter) mean.

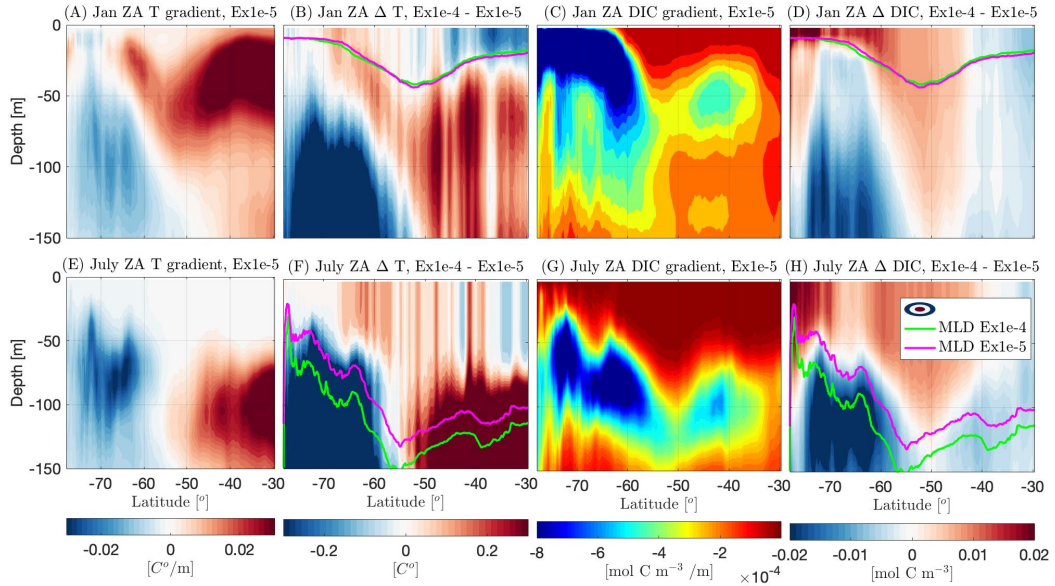


Figure 7: (A) January zonally averaged temperature vertical gradient (red implies increase in temperature towards the surface). (B) January change in temperature (Ex1e-4 - Ex1e-5). Mixed layer depth (MLD) for Ex1e-5 (pink) and Ex1e-4 (green) overlain. (C) January zonally averaged DIC vertical gradient. (D) Change in DIC concentration (Ex1e-4 - Ex1e-5). (E-H) As in A-D but for July mean.

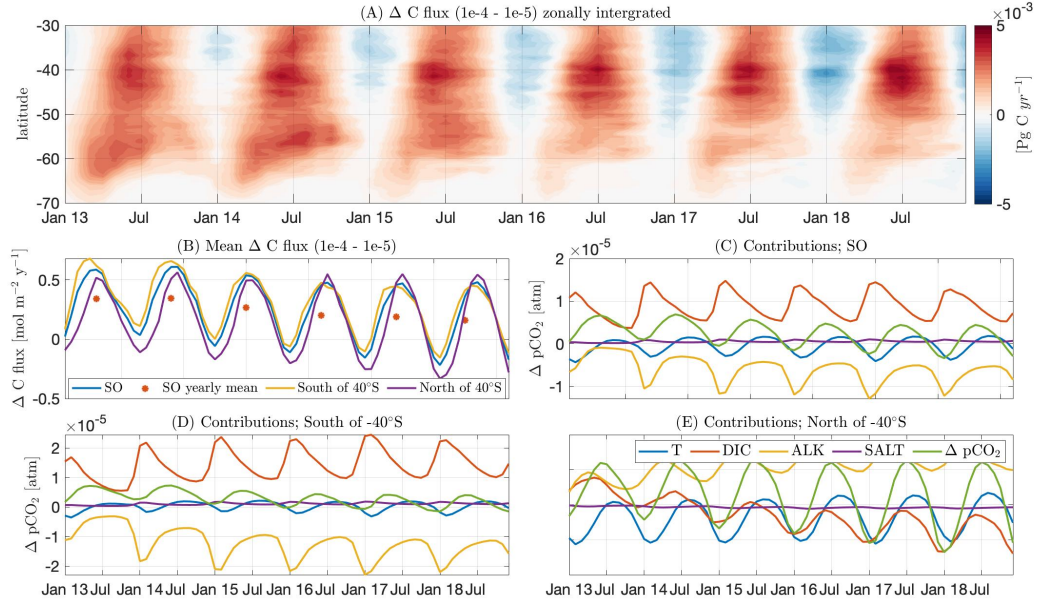


Figure 8: (A) Change in zonally integrated Carbon flux between Ex1e-4 and Ex1e-5 over the six-year time period of Jan 2013 to Dec 2018 (Red shows reduced uptake or increased outgassing in Ex1e-4). (B) Change in the mean carbon flux across the whole SO (blue), the SO North of $40^\circ S$ (purple) and South of $40^\circ S$ (yellow) for the same time period. The annual mean change for the whole SO for each year is shown (red star). Using the methodology of Takahashi et al. (2014) as discussed previously, the differences in Carbon flux between the two model runs over time can be attributed to changes in surface ocean pCO_2 (green lines) from alterations to temperature (blue lines), DIC (red lines), alkalinity (yellow lines) and salinity (purple lines). These contributions are shown for the whole SO (C), the SO south of $40^\circ S$ (D), and the SO north of $40^\circ S$ (E).

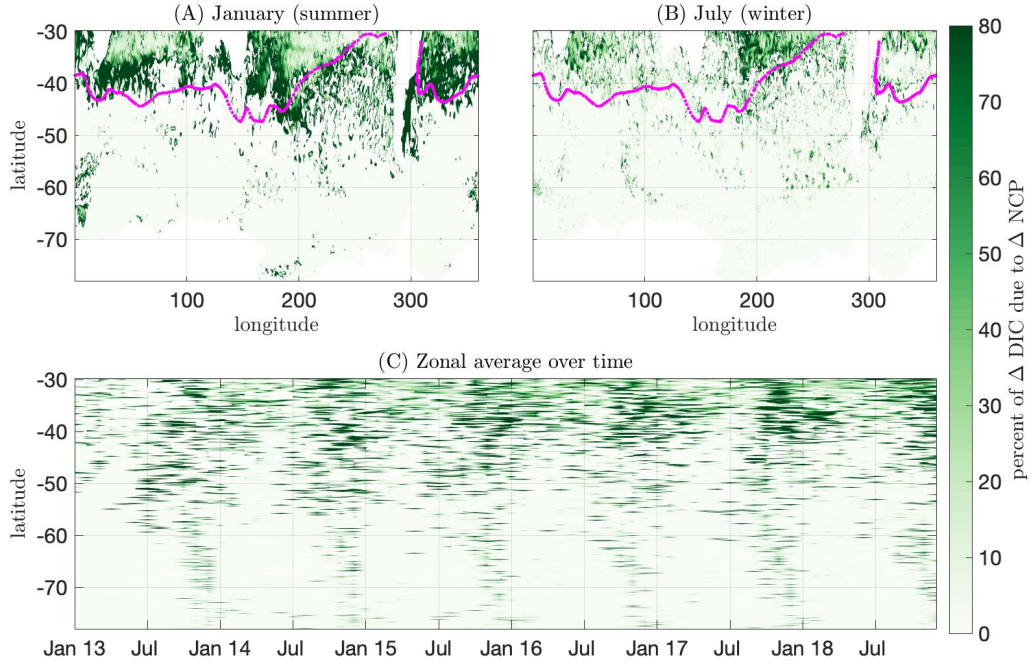


Figure 9: The percentage change of surface water DIC concentration due to changes in biological net community productivity (NCP). Surface water is defined here as waters down to a depth of 55m. Shown as a vertically integrated mean for (A) January (summer) and (B) July (winter). The mean location of the subtropical front, as defined by Orsi et al. (1995), is also shown in pink. (C) The zonal mean of the vertically integrated percentage change due to altered NCP is shown over time.

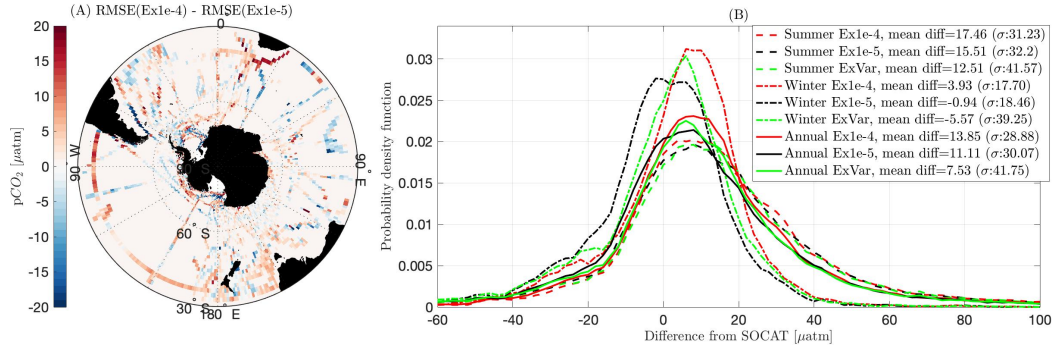


Figure 10: Comparison of modelled $p\text{CO}_2$ to observations from Surface Ocean CO_2 Atlas (SOCAT) between 2012 and 2018 (Bakker et al., 2016). (A) Comparison of the root mean squared error between Ex1e-4 and Ex1e-5. Red/blue shows regions where Ex1e-5/Ex1e-4 is closer to the observations. (B) Probability density function showing the misfit between observed carbon fluxes from SOCAT and the model outputs for $p\text{CO}_2$ in Ex1e-5 (black), Ex1e-4 (red), and ExVar (green).